Journal of Asian Earth Sciences 89 (2014) 108–122

Contents lists available at ScienceDirect

Journal of Asian Earth Sciences

journal homepage: www.elsevier.com/locate/jseaes

# Petrochemistry of ultrapotassic tephrites and associated cognate plutonic xenoliths with carbonatite affinities from the late Quaternary Qa'le Hasan Ali maars, central Iran

S. Saadat [a], C.R. Stern [b,*], A. Moradian [c]

[a] Department of Geology, Mashhad Branch, Islamic Azad University, Mashhad, Iran
[b] Department of Geological Sciences, University of Colorado, Boulder, CO, USA
[c] Department of Geology, Shahid Bahonar University, Kerman, Iran

ARTICLE INFO

*Article history:*
Received 27 August 2013
Received in revised form 24 March 2014
Accepted 25 March 2014
Available online 18 April 2014

*Keywords:*
Basanite tephrite
Carbonatite
Allanite
Britholite
Alpine–Himalayan collision belt
Iran

ABSTRACT

The Quaternary Qa'le Hasan Ali (QHA) maars in central Iran occur at the intersection of the north–south Nayband fault, which defines the western boundary of the Lut micro-continental block, and a system of northwest–southeast faults, subparallel to the Zagros suture zone, that formed during the Arabian–Eurasian collision. These post-collisional maars intrude Eocene volcanic rocks of the Urumieh–Dokhtar magmatic belt, which was generated by the subduction of Neotethys oceanic lithosphere below Iran. The highly potassic, Ti-phlogopite + Mg-rich ($Fo_{89-92}$) olivine + diopside-augite + aegirine–augite basanite tephrites forming the tuff rims of the QHA maars contain tephrite-coated plutonic xenoliths, some of which are interpreted as co-genetic with the tephrites based on their similar mineralogy and Sr isotopic composition ($^{87}Sr/^{86}Sr = 0.70590$). Cognate plutonic xenoliths have up to ~20 vol% calcite, considered to be magmatic calcite because of (1) its grain size, which is similar to feldspars and aegirine–augite pyroxenes in these rocks, (2) the occurrence of fine-grained inclusions of pyroxene and apatite within these calcite grains, and (3) the similarity of the Sr-isotopic composition of this calcite with the other minerals in these rocks. The fact that the magmatic calcite has remained intact and did not volatilize during the transport of these xenoliths to the surface in the hot tephrite magma implies a short transit time, indicating that they are samples of a shallow plutonic complex, as does the presence of anorthoclase in these plutonic xenoliths. Their high modal proportion of magmatic calcite suggests that this shallow plutonic complex has affinities with carbonatites. The magmatic calcite-bearing plutonic xenoliths have high LREE/HREE ratios and contain REE-rich allanite (with up to ~20 wt% LREE) and britholite (~60 wt% LREE) that make up ~3 modal percent of the most calcite-rich samples. Similar to many post-collisional highly potassic rocks formed in the Alpine–Himalayan collision zone, the highly potassic basanite tephrites of the QHA maars have high $^{87}Sr/^{86}Sr$ and low $\epsilon_{Nd}$ (−1.3 to −3.4), distinct from convecting asthenosphere, and they are depleted in Nb and Ta relative to Ba and La. They formed by small degrees of partial melting of lower continental lithospheric mantle metasomatized by both $H_2O$ and $CO_2$-rich fluids derived from subducted Neotethys oceanic crust and sediments during the collision of the Arabian and Eurasian plates.


## 1. Introduction

Milton (1976–77) described highly potassic tephrites associated with multiple late Quaternary maars, previously thought to be meteorite impact craters (Gojković, 1972), near the village of Qa'le (or Qal'eh) Hasan Ali (QHA; 29°24′N and 57°32′E; Figs. 1 and 2) in central Iran. Highly potassic post-collisional volcanic rocks occur at many localities along the Alpine–Himalayan collision belt, from Spain (Turner et al., 1999) to Tibet (Miller et al., 1999), as well as elsewhere in Iran (Ahmadzadeh et al., 2010; Pang et al., 2013). In the QHA tephrites, Milton observed phenocrysts of olivine, phlogopite and clinopyroxene in a groundmass containing phlogopite, anorthoclase, analcime, hauyne, clinopyroxene, magnetite and glass, but not plagioclase or leucite. Milton suggested that this "locality is worthy of further study for its significance in the Quaternary geologic development of Iran and for its petrologic peculiarities." In two subsequent studies, Sabzehei (1984) and Shishebore (1993) noted the similarity of these highly potassic alkaline rocks with either kamafugites (despite the absence of kalsilite) and/or the lamproite clan, respectively.

* Corresponding author. Tel.: +1 303 492 7170; fax: +1 303 492 2606.
*E-mail address:* Charles.Stern@colorado.edu (C.R. Stern).

http://dx.doi.org/10.1016/j.jseaes.2014.03.021
1367-9120/

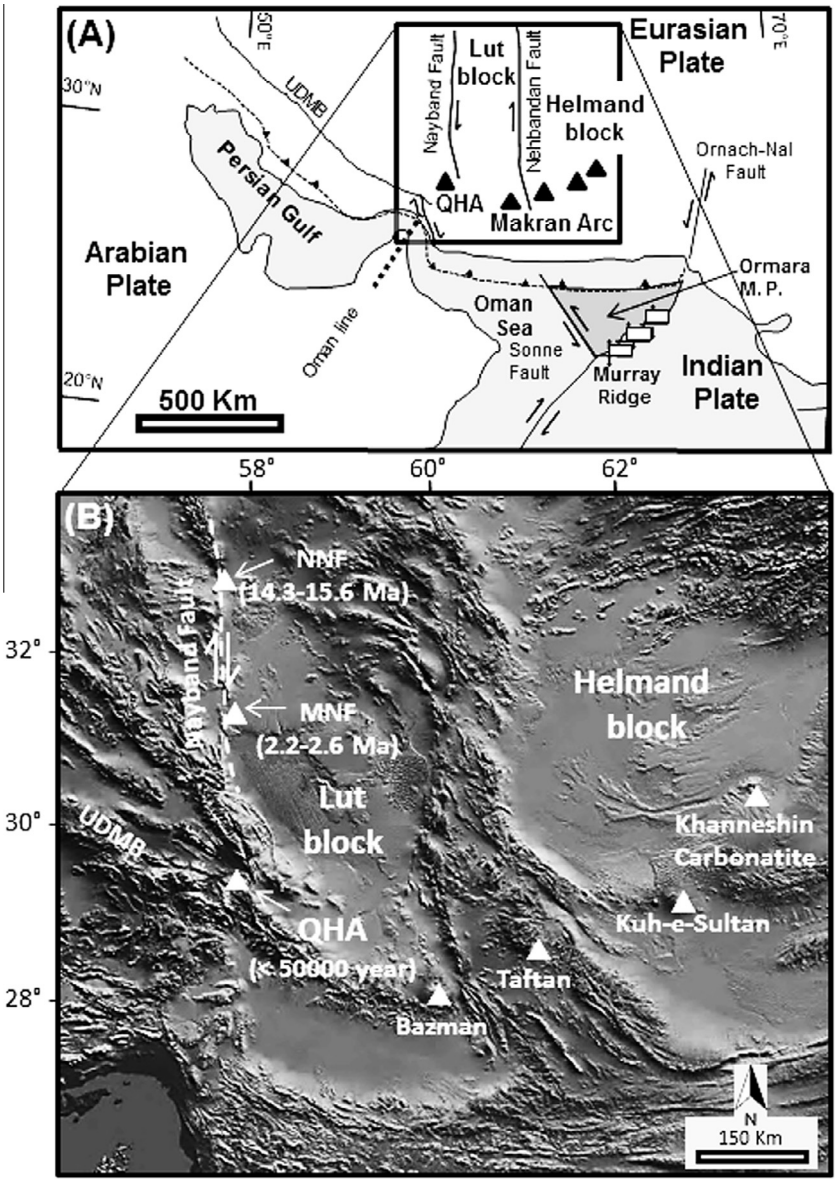


**Fig. 1.** (A) General tectonic setting of the southern part of eastern Iran showing the major plates and plate boundaries (McCall, 1997, 2002; Musson, 2009), faults, micro-continental blocks, the Tertiary Urumieh–Dokhtar magmatic belt (UDMB; Shafiei et al., 2009; Agard et al., 2011), the active Makran arc (Saadat and Stern, 2011), the Quaternary Khanneshin Carbonatite Complex in Afghanistan (Tucker et al., 2012), and the Qa'le Hasan Ali (QHA) maars (Milton, 1976–77). (B) Location map of the QHA maars at the intersection of the southern extension of the Nayband fault, which defines the western margin of the Lut block, and southeast–northwest trending faults parallel to the Zargo suture zone. The ages of other basaltic volcanic outcrops farther north along the Nayband fault (NNF and MNF) are also shown (Jung et al., 1984; Walker et al., 2009; Saadat et al., 2010; Pang et al., 2012), as are the location of the three major stratovolcanoes in the Makran arc (Saadat and Stern, 2011) and the Quaternary Khanneshin carbonatite complex in Afganistan (Mars and Rowan, 2011; Tucker et al., 2012).

Here we present new petrochemical information for samples collected from the QHA maars. These samples include both porphyritic, highly vesicular and glassy tephrite and less vesicular, granular, more nearly holocrystalline extrusive rocks, as well as cognate plutonic rocks, occurring as tephrite coated xenoliths, some containing up to >20% modal magmatic calcite and ~3% modal REE-rich allanite and britholite. Magmatic calcite also occurs in the groundmass of some of the granular extrusive samples, suggesting that these highly potassic alkaline rocks have certain affinities with carbonatites, as was originally proposed by Sabzehei (1984).

## 2. Geological setting

The QHA maars occur within the convergent orogen between the Arabian, Eurasian and Indian plates connecting the Alpine and Himalayan orogenic systems. The complex tectonic evolution of this area involves the closure of the Paleotethys ocean during collision with the Eurasian plate to the north, the closure of the Neotethys ocean during collision of the Arabian plate from the west, the closure of the Sistan ocean from the east, and ongoing subduction of the Oman oceanic plate from the south below the active Makran arc (Fig. 1; Berberian and King, 1981; Golonka, 2004; Shahabpour, 2005; Saadat and Stern, 2011). The maars occur along the intersection of the southern projection of the Nayband fault and a system of northwest-southeast trending faults, subparallel to the Zagros suture zone and Tertiary Urumieh–Dokhtar magmatic belt (UDMB; Fig. 1), associated with the Arabian-Eurasia collision and the closure of the Neotethys ocean (Shafiei et al., 2009; Agard et al., 2011). The north–south right-lateral strike-slip Nayband fault forms the western boundary of the Lut micro-continental block in eastern Iran. The northwest–southeast oriented

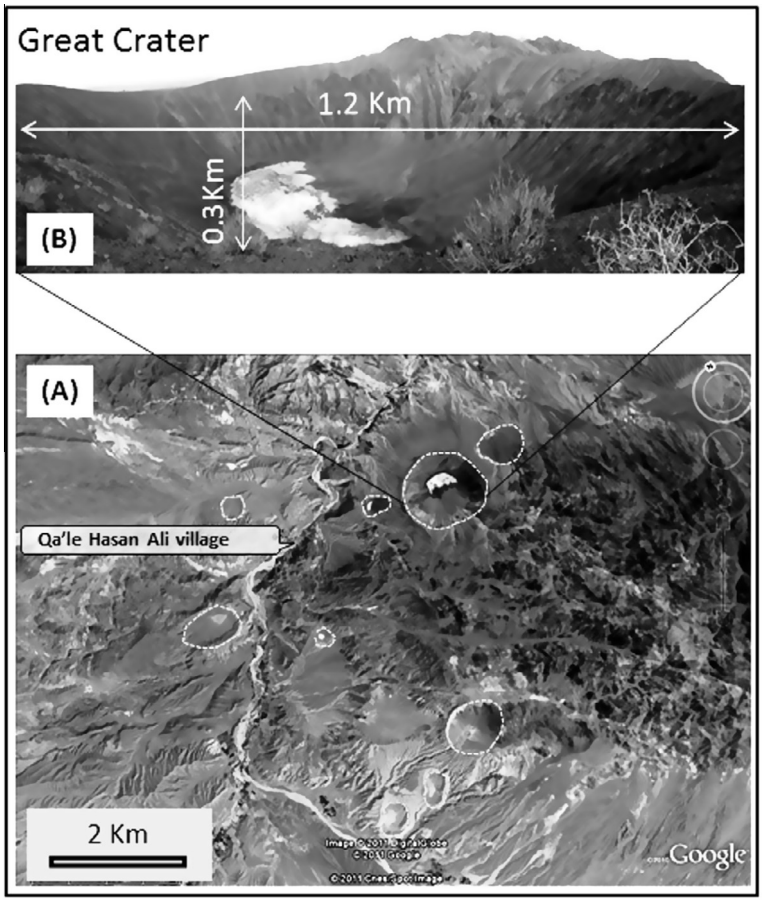


**Fig. 2.** (A) Image of the QHA maars. The borders of nine of the larger maars are indicated by dashed lines. (B) Photo of the inside of the 1.2 km in diameter and 300 m deep "Great Crater", the largest maar in the QHA field. The samples analyzed in this paper come from this maar. The white area inside the maar is salt.

fault system along which the QHA maars occur trends to the northwest towards the 11 Ma Saray volcano, formed by leucite-bearing ultrapotassic rock in northwestern Iran (Pang et al., 2013), and to the southeast into the Makran arc (Saadat and Stern, 2011), which continues to the east into Pakistan and to the northeast towards the Quaternary Khanneshin Carbonatite Complex in Afghanistan (Fig. 1; Mars and Rowan, 2011; Tucker et al., 2012).

Magmatic activity in the Lut block started in the late Jurassic and continued into the Quaternary (Esmaiely et al., 2005), forming a variety of volcanic and volcanoclastic rocks, as well as subvolcanic stocks and intrusive rocks. Extensive Tertiary magmatic activities in the Lut block have been described by Jung et al. (1984). Maximum volcanic activity on the Lut block took place at the end of the Eocene, contemporaneously with the most extensive and intense volcanic activity in other volcanic provinces of Iran (Berberian and King, 1981; Shahabpour, 2007; Verdel et al., 2011; Pang et al., 2012). The country rocks into which the QHA maars developed are Eocene calc-alkaline volcanic and plutonic rocks of the Urumieh–Dokhtar magmatic belt (UDMB; Fig. 1), which was generated by the subduction of the Neotethys ocean below the Eurasian continental crust of central Iran (Shafiei et al., 2009; Agard et al., 2011).

Neogene/Quaternary magmatic activity in the Lut microcontinental block extends over a south-to-north distance of 900 km, from the stratovolcanoes of the Makran arc along its southern margin (Farhoudi and Karig, 1977; Saadat and Stern, 2011) to the small monogenetic cones north of its northern margin (Saadat and Stern, 2012). From the Eocene and early Oligocene to the Neogene/Quaternary, there was a significant transition in composition and volume of volcanism, from mainly intermediate and felsic volcanic rocks with calc-alkaline characteristics to more limited mafic alkaline magmatism (Saadat, 2010; Karimpour et al., 2011; Verdel et al., 2011; Pang et al., 2012), except where active calc-alkaline arc volcanoes occur in the Makran arc. In conjunction with this transition, there was a migration, from north to the south, of Neogene/Quaternary volcanism with time, for alkali volcanic rocks that have erupted along the Nayband fault on the western margin of the Lut block (Fig. 1; Saadat et al., 2010). Geochronological data for these alkali olivine basalts yield ages of 15.6–14.3 Ma (Jung et al., 1984; Pang et al., 2012) for samples from the northern Nayband fault (NNF), and of 2.6–2.2 Ma (Walker et al., 2009) for samples from the middle part of the Nayband fault (MNF).

Farther south, along the southern projection of the Nayband fault, are located the late Quaternary QHA maars (Figs. 1 and 2). As suggested by Milton (1976–77), these may range from only 5000 to 50,000 years in age judging by their degree of erosion. They are clearly post-collisional, as are the ultrapotassic rocks of the 11 Ma Saray volcano in northwestern Iran (Pang et al., 2013). The largest of the 14 craters in the QHA volcanic field, the "Great Crater", samples from which are the focus of this paper, has a diameter of about 1200 m and a depth around 200–300 m (Fig. 2).

## 3. Methods

Samples were collected from the Great Crater. Mineral compositions, including REE in allanite and britholite, were analyzed using the JEOL, JXA-8600 super probe, in the Laboratory for

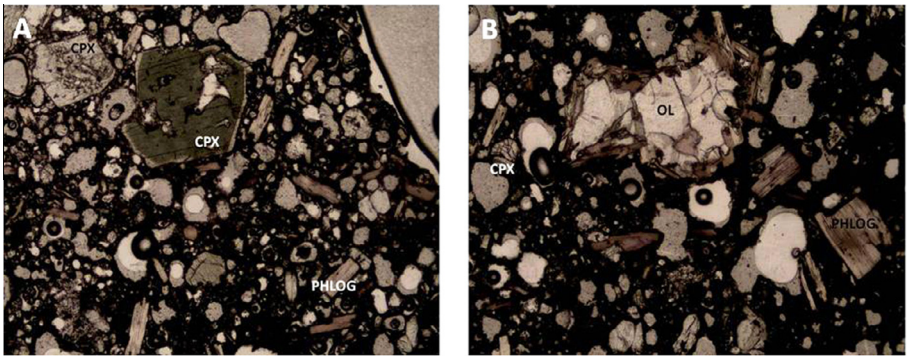


**Fig. 3.** Photomicrographs of glassy vesicular porphyritic tephrite sample M4. (A) Phenocrysts of pale-green Na-rich salite and colorless diopside/augite clinopyroxene (CPX), along with phlogopite (PHLOG), in a dark glassy groundmass with pyroxene, phlogopite, magnetite and minor alkali feldspar, analcime and hueyne. (B) Phenocrysts of Mg-olivine (OL) rimmed by phlogopite, phlogopite and colorless diopside/augirine clinopyroxene in the same sample (plane polarized light; field of view 2.3 × 1.9 mm).

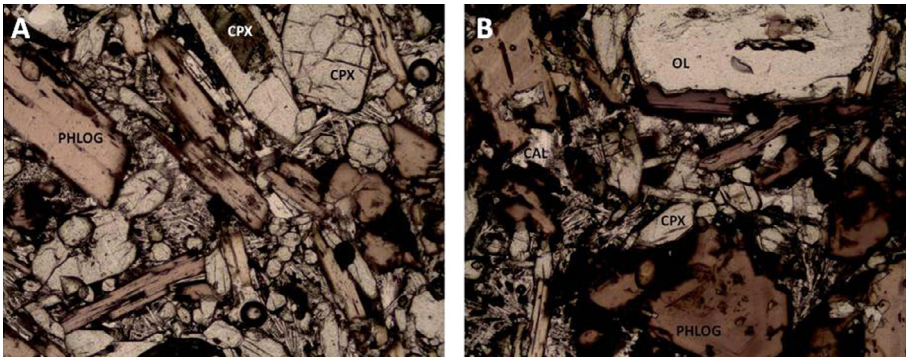


**Fig. 4.** Photomicrographs of granular nearly holocrystalline extrusive sample M1. (A) Phenocrysts of phlogopite and colorless diospide/augite clinopyroxene, next to another with a green Na-rich core, in a groundmass of finer grained phlogopite, pyroxene, and minor calcite, magnetite, analcime, sanadine and hueyne. (B) Phenocryst of phlogopite and Mg-rich olivine rimmed by phlogopite, in a groundmass of finer grained calcite (CAL), pyroxenes, magnetite, sanadine, analcime and hueyne (plane polarized light; field of view 2.3 × 1.9 mm).

**Table 1**
Compositions of olivine phenocrysts from Qa'le Hasan Ali basanite tephrites and Neogene/Quaternary Alkali olivine basalt samples from farther north along the Nayband fault.

| Location | Qa'le Hasan Ali | | | | | | | MNF[a] | NNF[b] |
|---|---|---|---|---|---|---|---|---|---|
| | Tephrite | | | | | | | Basalt | |
| | M-1 | M-3 | M-4 | | M-14 | M-15 | | Average[c] | |
| | Core | Core | Core | Rim | Core | Core | Rim | Core | Core |
| No. | 3 | 4 | 3 | 1 | 5 | 5 | 1 | 3 | 11 |
| $SiO_2$ | 41.3 | 42.0 | 40.9 | 41.2 | 41.9 | 41.7 | 41.3 | 39.4 | 39.9 |
| FeO | 8.2 | 9.2 | 8.7 | 10.2 | 10.4 | 7.8 | 7.5 | 19.9 | 22.4 |
| MnO | 0.1 | 0.1 | 0.2 | 0.1 | 0.2 | 0.1 | 0.1 | 0.2 | 0.3 |
| NiO | 0.5 | 0.4 | 0.4 | 0.4 | 0.3 | 0.5 | 0.5 | 0.1 | 0.1 |
| MgO | 50.7 | 50.2 | 50.3 | 49.5 | 49.1 | 51.0 | 50.9 | 41.1 | 38.9 |
| Total | 100.8 | 101.9 | 101.0 | 101.4 | 101.9 | 101.0 | 100.3 | 100.8 | 101.8 |
| *Cations calculated on the basis of 4 oxygens* | | | | | | | | | |
| Fe | 0.17 | 0.18 | 0.18 | 0.21 | 0.21 | 0.16 | 0.15 | 0.43 | 0.32 |
| Mn | 0 | 0 | 0 | 0 | 0 | 0 | 0 | 0.01 | 0 |
| Ni | 0.01 | 0.01 | 0.01 | 0.01 | 0.01 | 0.01 | 0.01 | 0 | 0 |
| Mg | 1.82 | 1.80 | 1.82 | 1.79 | 1.77 | 1.83 | 1.83 | 1.56 | 0.99 |
| Fo | 92 | 91 | 91 | 89 | 89 | 92 | 92 | 78 | 75 |

[a] MNF = Middle Nayband fault.
[b] NNF = Northern Nayband fault.
[c] (Saadat et al., 2010).

Environmental and Geological Science (University of Colorado at Boulder), with an electron gun accelerating voltage of 15 kV (25 kV for the REE-rich minerals), current range from 17 to 24 nA, and a one to five micron diameter focused beam. Matrix correction was done by J. Armstrong's ZAF correction program using natural mineral standards.

Rock samples were powdered for whole-rock geochemical analysis. Portions of these rock powders were sent to the X-Ray Fluorescence (XRF) laboratory in Ferdowsi University of Mashhad (Iran), where a Philips (X, Unique II) instrument was used for measuring the major elements. Trace-elements contents were determined by ICP-MS (Inductively Coupled Plasma Mass

**Table 2**
Composition of clinopyroxenes in Qa'le Hasan Ali samples.

| Rock type | Tephrite | | | | | | | | | Cognate plutonic xenoliths | | |
|---|---|---|---|---|---|---|---|---|---|---|---|---|
| Sample | M-1 | | | M-4 | | | M-15 | | | M-11 | M-8 | M-9 |
| | Core | Rim | Small grain | Core | Rim | Small grain | Core | Rim | Small grain | No zonation | No zonation | No zonation |
| No. | 3 | 3 | 2 | 1 | 1 | 6 | 2 | 3 | 5 | 10 | 6 | 4 |
| $SiO_2$ | 50.84 | 53.54 | 52.55 | 47.56 | 51.6 | 50.23 | 48.71 | 52.83 | 53.27 | 46.45 | 46.79 | 48.37 |
| $Al_2O_3$ | 2.36 | 1.55 | 0.87 | 4.12 | 1.56 | 3.64 | 4.60 | 2.35 | 2.19 | 4.87 | 3.51 | 4.86 |
| $TiO_2$ | 0.50 | 0.40 | 1.17 | 0.47 | 0.33 | 0.50 | 0.57 | 0.48 | 0.47 | 0.54 | 0.36 | 0.70 |
| $Cr_2O_3$ | 0.01 | 0.08 | 0.02 | 0.04 | 0.00 | 0.05 | 0.02 | 0.06 | 0.05 | 0.01 | 0.01 | 0.00 |
| FeO | 10.72 | 3.39 | 5.28 | 15.96 | 4.58 | 8.43 | 15.8 | 4.45 | 3.80 | 18.27 | 19.59 | 10.96 |
| MnO | 0.36 | 0.07 | 0.10 | 0.50 | 0.13 | 0.22 | 0.67 | 0.09 | 0.09 | 1.09 | 0.84 | 0.23 |
| MgO | 11.46 | 17.15 | 15.83 | 7.20 | 16.21 | 12.78 | 7.20 | 15.97 | 16.86 | 5.50 | 5.15 | 10.13 |
| CaO | 22.78 | 24.03 | 23.67 | 20.63 | 23.45 | 22.22 | 20.55 | 23.35 | 22.89 | 20.23 | 20.08 | 22.04 |
| $Na_2O$ | 0.87 | 0.25 | 0.34 | 1.73 | 0.30 | 0.94 | 1.88 | 0.41 | 0.38 | 1.94 | 1.96 | 1.35 |
| Total | 99.91 | 100.45 | 99.83 | 98.21 | 98.18 | 99.02 | 100 | 100 | 100 | 98.88 | 98.29 | 98.63 |
| *Cations calculated on the basis of 6 oxygen* | | | | | | | | | | | | |
| Si | 1.90 | 1.94 | 1.94 | 1.86 | 1.92 | 1.90 | 1.86 | 1.93 | 1.94 | 1.81 | 1.85 | 1.84 |
| Al | 0.10 | 0.07 | 0.04 | 0.20 | 0.07 | 0.20 | 0.21 | 0.10 | 0.09 | 0.22 | 0.16 | 0.22 |
| Ti | 0.01 | 0.01 | 0.03 | 0.01 | 0.01 | 0.01 | 0.02 | 0.01 | 0.01 | 0.02 | 0.01 | 0.02 |
| Cr | 0.00 | 0.00 | 0.00 | 0.00 | 0.00 | 0.00 | 0.00 | 0.00 | 0.00 | 0.00 | 0.00 | 0.00 |
| Fe | 0.34 | 0.11 | 0.16 | 0.52 | 0.14 | 0.27 | 0.51 | 0.14 | 0.12 | 0.60 | 0.65 | 0.35 |
| Mn | 0.01 | 0.00 | 0.00 | 0.02 | 0.00 | 0.01 | 0.02 | 0.00 | 0.00 | 0.04 | 0.03 | 0.01 |
| Mg | 0.64 | 0.93 | 0.87 | 0.42 | 0.90 | 0.71 | 0.41 | 0.87 | 0.91 | 0.32 | 0.30 | 0.57 |
| Ca | 0.92 | 0.94 | 0.94 | 0.86 | 0.94 | 0.90 | 0.84 | 0.91 | 0.9 | 0.85 | 0.85 | 0.90 |
| Na | 0.06 | 0.02 | 0.03 | 0.13 | 0.02 | 0.07 | 0.14 | 0.03 | 0.03 | 0.15 | 0.15 | 0.10 |
| En | 34 | 48 | 44 | 23 | 46 | 41 | 23 | 45 | 48 | 18 | 17 | 32 |
| Wo | 48 | 47 | 48 | 48 | 47 | 51 | 48 | 48 | 46 | 48 | 47 | 49 |
| Fs | 18 | 5 | 8 | 29 | 7 | 8 | 29 | 7 | 6 | 34 | 36 | 19 |

**Table 3**
Compositions of feldspar in Qa'le Hasan Ali samples.

| Rock type | Tephrite | | Cognate plutonic xenoliths | | | | | |
|---|---|---|---|---|---|---|---|---|
| Sample | M-15 | M-1 | M-11 | | M-8 | | M-9 | |
| No. | 2 | 5 | 7 | 7 | 4 | 4 | 5 | 3 |
| $SiO_2$ | 64.3 | 63.7 | 62.6 | 62.9 | 61.5 | 63.6 | 58.4 | 60.2 |
| $Al_2O_3$ | 19.4 | 20.4 | 22.4 | 21.2 | 22.8 | 19.7 | 24.9 | 20.8 |
| FeO | 0.2 | 0.4 | 0.3 | 0.4 | 0.3 | 0.2 | 0.2 | 0.1 |
| CaO | 0.3 | 0.5 | 3.0 | 1.8 | 3.7 | 0.6 | 5.5 | 1.0 |
| $Na_2O$ | 1.8 | 2.8 | 6.8 | 5.9 | 8.4 | 4.9 | 7.1 | 4.1 |
| $K_2O$ | 14.5 | 12.5 | 3.6 | 6.2 | 1.5 | 9.4 | 1.5 | 8.7 |
| Total | 100.4 | 100.2 | 98.8 | 98.3 | 98.2 | 98.4 | 97.6 | 95.0 |
| *Number of ions on basis of 32 oxygens* | | | | | | | | |
| Si | 11.75 | 11.40 | 11.36 | 11.49 | 11.10 | 11.66 | 10.67 | 11.47 |
| Al | 4.18 | 4.45 | 4.79 | 4.57 | 4.85 | 4.26 | 5.36 | 4.67 |
| Fe | 0.04 | 0.10 | 0.04 | 0.05 | 0.04 | 0.03 | 0.03 | 0.02 |
| Ca | 0.04 | 0.09 | 0.59 | 0.36 | 0.72 | 0.12 | 1.08 | 0.21 |
| Na | 0.62 | 1.00 | 2.39 | 2.07 | 2.95 | 1.74 | 2.51 | 1.51 |
| K | 3.38 | 2.96 | 0.83 | 1.45 | 0.35 | 2.20 | 0.35 | 2.12 |
| Or | 84 | 73 | 22 | 37 | 9 | 54 | 9 | 55 |
| Ab | 15 | 25 | 63 | 54 | 73 | 43 | 64 | 39 |
| An | 1 | 2 | 15 | 9 | 18 | 3 | 27 | 6 |

**Table 4**
Compositions of phlogopite in the Qa'le Hasan Ali samples.

| Sample | M-3 | M-15 | | M-4 | M-14 | M-1 | M-5 |
|---|---|---|---|---|---|---|---|
| No. | Core 2 | Core 3 | Rim 2 | Core 2 | Core 2 | Core 2 | Core 2 |
| $SiO_2$ | 37.9 | 38.3 | 35.3 | 36.5 | 37.5 | 37.7 | 39.2 |
| $TiO_2$ | 2.6 | 2.6 | 3.2 | 2.7 | 3.0 | 3.1 | 1.9 |
| $Al_2O_3$ | 14.7 | 14.8 | 14.8 | 14.7 | 15.4 | 15.4 | 13.2 |
| FeO | 7.6 | 8.2 | 17.2 | 7.5 | 7.8 | 4.4 | 6.2 |
| MnO | 0.1 | 0.05 | 0.3 | 0.1 | 0 | 0 | 0 |
| MgO | 21.2 | 20.9 | 14.1 | 20.4 | 20 | 21.7 | 23.1 |
| CaO | 0.1 | 0.1 | 0 | 1.9 | 0 | 0 | 0 |
| $Na_2O$ | 0.3 | 0.25 | 0.4 | 0.3 | 0.3 | 0.2 | 0.1 |
| $K_2O$ | 9.7 | 9.7 | 9.1 | 9.6 | 9.3 | 10.1 | 10.2 |
| F | 3.1 | 3.05 | 2.9 | 3.1 | 3.1 | 3.1 | 3.1 |
| Cl | 0 | 0 | 0 | 0 | 0 | 0 | 0 |
| Total | 95.9 | 96.5 | 96.1 | 95.5 | 95.3 | 94.5 | 95.7 |
| *Number of cations on the basis of 22 oxygenes* | | | | | | | |
| Si | 5.61 | 5.65 | 5.48 | 5.44 | 5.62 | 5.62 | 5.75 |
| Al | 2.56 | 2.58 | 2.71 | 2.58 | 2.72 | 2.7 | 2.28 |
| Ti | 0.28 | 0.29 | 0.37 | 0.30 | 0.34 | 0.34 | 0.2 |
| Fe | 0.95 | 1.01 | 2.23 | 0.94 | 0.98 | 0.55 | 0.76 |
| Mn | 0.01 | 0.01 | 0.04 | 0.01 | 0.01 | 0 | 0.01 |
| Mg | 4.67 | 4.59 | 3.25 | 4.52 | 4.47 | 4.81 | 5.06 |
| Ca | 0.01 | 0 | 0 | 0.32 | 0 | 0 | 0 |
| Na | 0.08 | 0.07 | 0.11 | 0.09 | 0.09 | 0.06 | 0.04 |
| K | 1.84 | 1.82 | 1.81 | 1.82 | 1.78 | 1.91 | 1.9 |
| F | 1.43 | 1.42 | 1.44 | 1.46 | 1.45 | 1.47 | 1.42 |
| Cl | 0.01 | 0.01 | 0.01 | 0.01 | 0.01 | 0.01 | 0 |

Spectrometry) using an ELAN DCR-E instrument in the Department of the Geological Science, University of Colorado at Boulder, and also were obtained for some samples through a commercial ICP-MS laboratory (Activation Laboratories). USGS standards were used as the calibration standards and precision for analytical technique is generally better than 5% at the 95% confidence level (Saadat and Stern, 2012).

Isotopic measurements were carried out on leached whole-rock material using a Finnigan-Mat 261 six collector thermal ionization mass-spectrometer in the Department of the Geological Science, University of Colorado at Boulder. Details of analytical procedures are given in Saadat and Stern (2012). In addition, the leachate, calcite and anorthoclase from one plutonic rock sample (M11; Table 8) were analyzed for Sr isotopic composition. Separation of the calcite and anorthoclase were done by computer-controlled micro-drilling techniques using a Leica GZ6 Merchantek microscope for high resolution sampling.

## 4. Results

### 4.1. Petrography and mineral chemistry

#### 4.1.1. Extrusive rocks

Sample of extrusive rocks collected from the Great Crater in the maar field near the village of Qa'le Hasan Ali include highly

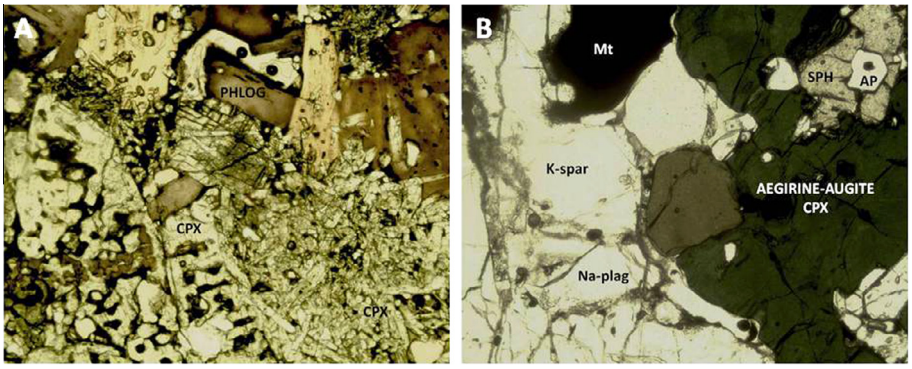


**Fig. 5.** Photomicrograph of two plutonic xenoliths. (A) Phlogopite-pyroxenite sample M5, containing large pyroxene grains, commonly with sieve texture, as well as acicular pyroxenes, both poikilitic and non-poikilitic phlogopite grains, minor apatite, magnetite and anorthoclase. Milton (1976–77) suggested that samples similar to this were cumulates. (B) Holocrystalline two-feldspar pyroxenite sample M8 with dark green aegirine–augite clinopyroxene, K-feldspar, Na-plagioclase, sphene (SPH), apatite (AP) and magnetite (Mt) (plane polarized light; field of view 2.3 × 1.9 mm).

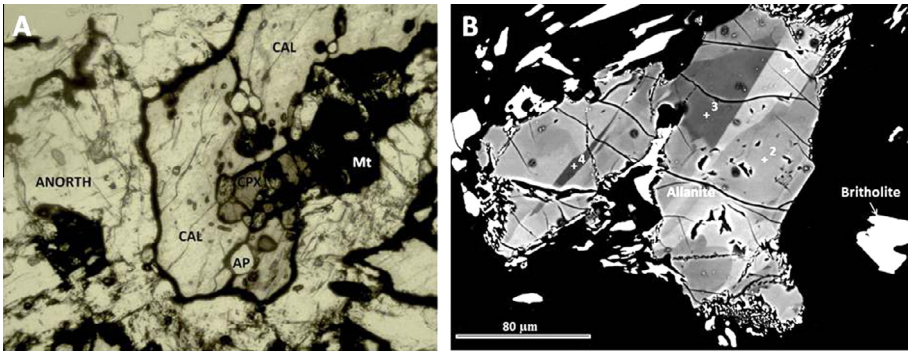


**Fig. 6.** Photomicrograph of calcite-bearing anorthoclase–pyroxenite plutonic xenolith M11. (A) Photo showing the presence of small grains of apatite (AP) and clinopyroxene within calcite (CAL) crystals, indicating co-crystallization of the different phases in this sample and suggesting that calcite is a primary igneous phase, not a secondary or replacement phase. Sample also contains sphene (SPH) and magnetite (Mt) (plane polarized light; field of view 2.3 × 1.9 mm). (B) Back-scattered electron image of allanite (Grain #1; Table 6) and britholite in calcite-bearing plutonic xenoliths sample M11. Image shows the different internal compositional domains of the allanite grain, with the brighter areas being more REE-rich. Numbers indicate the location of the points analyzed (Table 6).

**Table 5**
Composition of amphibole in a cognate xenoliths.

| Sample | M-9 | | |
|---|---|---|---|
| Rock type | Plutonic xenoliths | | |
| No. | 6 | | |
| $SiO_2$ | 37.15 | Number of ions on basis of 23 oxygens | |
| $TiO_2$ | 2.09 | Si | 5.86 |
| $Al_2O_3$ | 14.16 | Ti | 0.25 |
| FeO | 16.31 | Al | 2.63 |
| MnO | 0.21 | Fe | 2.15 |
| MgO | 9.34 | Mn | 0.03 |
| CaO | 11.42 | Mg | 2.20 |
| $Na_2O$ | 1.86 | Ca | 1.93 |
| $K_2O$ | 2.40 | Na | 0.57 |
| Cl | 0.04 | K | 0.48 |
| F | 0.33 | Cl | 0.01 |
| Total | 95.28 | F | 0.15 |

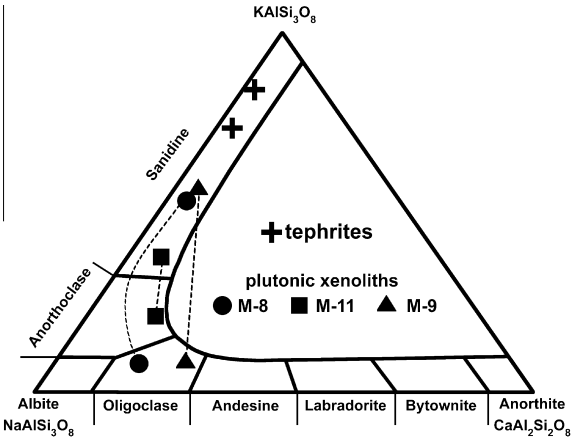


**Fig. 7.** Triangular Ca–Na–K diagram showing the compositions of the feldspars in the extrusive tephrites of the QHA maars and cognate plutonic xenoliths they contain.

vesicular, glassy, porphyritic types (samples M4 and M14 in the tables; Fig. 3), as well as denser, nearly holocrystalline, granular types (samples M1, M3 and M15 in the tables; Fig. 4). Vesicular, glassy, porphyritic types contain phenocrysts of olivine, phlogopite, colorless diopside-augite and pale to dark green aegirine–augite clinopyroxene in a glassy vesiculated groundmass with pyroxene, magnetite, analcime, huayne, and alkali feldspar. The denser, nearly holocrystalline, granular samples contain a greater proportion of phlogopite phenocrysts, along with olivine, diopside/augite and aegirine–augite clinopyroxene phenocrysts in a groundmass of sanidine, phlogopite, pyroxene, magnetite and apatite, with minor amounts of analcime, hauyne, calcite and glass concentrated between phenocrysts (Fig. 4) or along the edges of vesicles. No plagioclase feldspar, leucite, kalsilite or melilite occurs in any of these rocks.

**Table 6**
Compositions of allanite and britholite in calcite-bearing plutonic xenoliths M11, with molecular formulas calculate according to method #10 of Ercit (2002).

| Grain/point | Aln #1-1 | Aln #1-2 | Aln #1-3 | Aln #1-4 | Aln #2-1 | Aln #2-2 | Aln ave | Britholite |
|---|---|---|---|---|---|---|---|---|
| $SiO_2$ | 31.41 | 31.27 | 32.52 | 32.71 | 32.01 | 32.68 | 32.10 | 22.86 |
| $TiO_2$ | 0.64 | 0.59 | 0.59 | 0.54 | 0.68 | 0.42 | 0.58 | 0.00 |
| $ThO_2$ | 0.89 | 0.81 | 0.59 | 0.78 | 0.81 | 0.46 | 0.72 | 3.29 |
| $Al_2O_3$ | 14.93 | 16.06 | 16.24 | 16.72 | 14.96 | 16.75 | 15.94 | 0.00 |
| $La_2O_3$ | 6.35 | 5.36 | 5.23 | 4.36 | 5.81 | 5.13 | 5.37 | 17.76 |
| $Ce_2O_3$ | 9.79 | 9.39 | 8.44 | 7.92 | 9.36 | 8.50 | 8.90 | 30.92 |
| $Pr_2O_3$ | 0.88 | 0.89 | 0.86 | 0.79 | 0.88 | 0.80 | 0.85 | 2.62 |
| $Nd_2O_3$ | 2.22 | 2.64 | 2.44 | 2.42 | 2.35 | 2.39 | 2.41 | 8.42 |
| $Sm_2O_3$ | 0.11 | 0.17 | 0.12 | 0.16 | 0.15 | 0.20 | 0.15 | 0.41 |
| $Dy_2O_3$ | 0.15 | 0.12 | 0.11 | 0.13 | 0.13 | 0.12 | 0.13 | 0.06 |
| $Fe_2O_3$ | 10.81 | 12.72 | 11.36 | 11.21 | 10.94 | 11.25 | 11.38 | 0.34 |
| FeO | 6.17 | 3.75 | 4.95 | 4.82 | 6.46 | 4.77 | 5.15 | 0.00 |
| MgO | 0.51 | 0.47 | 0.52 | 0.46 | 0.44 | 0.43 | 0.47 | 0.00 |
| MnO | 0.53 | 0.46 | 0.51 | 0.47 | 0.53 | 0.49 | 0.50 | 0.00 |
| CaO | 12.56 | 12.82 | 13.86 | 14.46 | 12.82 | 13.92 | 13.41 | 13.31 |
| $H_2O$ | 1.59 | 1.60 | 1.64 | 1.65 | 1.62 | 1.66 | 1.63 | 1.02 |
| F | <0.09 | <0.09 | <0.09 | <0.09 | <0.09 | <0.09 | | 0.25 |
| O = F | | | | | | | | −0.11 |
| TOTAL | 100.08 | 100.08 | 99.95 | 99.67 | 100.00 | 99.96 | 99.89 | 101.43 |
| Si | 2.967 | 2.950 | 2.977 | 2.975 | 2.959 | 2.960 | 2.965 | 3.004 |
| Ti | 0.042 | 0.040 | 0.040 | 0.037 | 0.047 | 0.029 | 0.039 | |
| Al (IV) | | 0.010 | | | | 0.012 | 0.004 | |
| Total T | 3.009 | 3.000 | 3.017 | 3.012 | 3.007 | 3.000 | 3.008 | 3.004 |
| Al (VI) | 1.630 | 1.710 | 1.729 | 1.768 | 1.630 | 1.776 | 1.707 | |
| $Fe^{3+}$ | 0.759 | 0.796 | 0.747 | 0.767 | 0.761 | 0.766 | 0.766 | 0.034 |
| $Fe^{2+}$ | 0.488 | 0.393 | 0.379 | 0.367 | 0.499 | 0.361 | 0.415 | |
| $Mn^{2+}$ | 0.042 | 0.036 | 0.039 | 0.036 | 0.041 | 0.037 | 0.039 | |
| Mg | 0.072 | 0.065 | 0.070 | 0.062 | 0.061 | 0.058 | 0.065 | |
| Total M | 2.991 | 3.000 | 2.983 | 3.000 | 2.993 | 3.000 | 2.992 | |
| Ca | 1.271 | 1.284 | 1.359 | 1.410 | 1.270 | 1.351 | 1.324 | 1.874 |
| La | 0.221 | 0.185 | 0.177 | 0.146 | 0.198 | 0.171 | 0.183 | 0.861 |
| Ce | 0.339 | 0.321 | 0.283 | 0.264 | 0.317 | 0.282 | 0.301 | 1.487 |
| Pr | 0.030 | 0.030 | 0.029 | 0.026 | 0.030 | 0.026 | 0.029 | 0.125 |
| Nd | 0.075 | 0.088 | 0.080 | 0.079 | 0.078 | 0.077 | 0.079 | 0.395 |
| Sm | 0.007 | 0.012 | 0.008 | 0.011 | 0.010 | 0.013 | 0.011 | 0.019 |
| Dy | 0.005 | 0.004 | 0.003 | 0.004 | 0.004 | 0.003 | 0.004 | 0.003 |
| Th | 0.019 | 0.017 | 0.012 | 0.016 | 0.017 | 0.010 | 0.015 | 0.098 |
| Total A | 1.968 | 1.949 | 1.957 | 1.968 | 1.943 | 1.943 | 1.955 | 4.912 |
| TOTAL | 7.968 | 7.949 | 7.957 | 7.968 | 7.943 | 7.943 | 7.955 | 10.920 |
| H | 1.000 | 1.000 | 1.000 | 1.000 | 1.000 | 1.000 | 1.000 | 0.896 |
| F | | | | | | | | 0.104 |
| O | 13.000 | 13.000 | 13.000 | 13.000 | 13.000 | 13.000 | 13.000 | 13.000 |
| Vacancy | 0.032 | 0.051 | 0.043 | 0.032 | 0.057 | 0.057 | 0.045 | |

Olivine phenocrysts within both the porphyritic glassy vesicular and granular holocrystaline rocks are homogeneous, with Mg-rich compositions ranging from $Fo_{89-92}$ (Table 1). Small grains of chromium spinel are present within some olivine phenocrysts. Olivines are rarely euhedral, but more often embayed and rimmed by phlogopite (Figs. 3 and 4). Clinopyroxenes have a wide range of appearance, from colorless diopsode/augite to pale to deep green Na-rich salite and/or aegirine–augite, and composition, with FeO varying from 3.4 to 16 wt% in conjunction with increases in $Na_2O$ from 0.25 to 1.9 wt% and $Al_2O_3$ from 0.9 to 4.6 wt% (Table 2). Zoned clinopyroxenes include both those with colorless diopside/augite centers and green Na-rich rims, or with pale to dark green Na-rich cores and colorless rims (Figs. 3 and 4). Feldspars in the groundmass are sanidine, not anorthoclase (Table 3).

In both the porphyritic, glassy, vesicular samples and the denser, more nearly holocyrstalline, granular samples, phlogopite occurs as phenocrysts, as a groundmass phase, and also as coronas around olivine (Figs. 3 and 4). Phlogopite phenocrysts are generally homogeneous, with a restricted range in composition, containing 2.6–3.1 wt% $TiO_2$ and 7.6–8.2 wt% FeO (Table 4). Occasionally phlogopite phenocrysts have rims that are more $TiO_2$ and FeO-rich (sample M15; Table 4). Both groundmass phlogopite and phlogopite forming coronas around olivines do not differ in composition from that of the cores of associated phlogopite phenocryst.

*4.1.2. Cognate plutonic xenoliths*

Cognate plutonic rocks occur as rounded tephrite coated xenoliths up to 15 cm in diameter in the extrusive rocks that form the wall of the Great Crater. They contain diopside/augite and/or aegirine–augite clinopyroxene, phlogopite, alkali feldspars and Na-plagioclase, apatite, magnetite, sphene, zircon, occasional amphibole, allanite and britholite, and in some cases up to >20% modal calcite, which as discussed in more detail below, we interpret as magmatic calcite (Figs. 5 and 6).

Four different samples of these rounded tephrite-covered plutonic xenoliths were analyzed. One, a phlogopite pyroxenite (sample M5; Fig. 5A), is similar to samples described by Milton (1976–77) as possible cumulates. It consists of both phlogopite

**Table 7**
Major element (wt%) and trace element (ppm) compositions of samples from Qa'le Hasan Ali maars and Neogene/Quaternary alkali olivine basalts from farther north along the Nayband fault (Saadat et al., 2010).

| Location | Qa'le Hasan Ali | | | | | | | | | | MNF | NNF |
|---|---|---|---|---|---|---|---|---|---|---|---|---|
| Rock type | Extrusives | | | | | | Plutonics | | | | Basalt | Basalt |
| Sample | M1 | M-3 | M-4 | M-14 | M-15 | Prev[a] | M-5 | M-8 | M-9 | M-11 | Ave. | Ave. |
| $SiO_2$ | 42.1 | 42.6 | 45.4 | 47.4 | 45.8 | 43.7 | 42.9 | 52.8 | 43.5 | 54.9 | 47.3 | 50.9 |
| $TiO_2$ | 1.4 | 1.6 | 1.0 | 0.9 | 1.2 | 1.3 | 0.8 | 0.3 | 1.0 | 0.2 | 2.8 | 2.2 |
| $Al_2O_3$ | 9.9 | 10.2 | 12.6 | 12.4 | 11.8 | 10.4 | 6.2 | 10.0 | 11.4 | 18.7 | 13.9 | 14.7 |
| FeO | 7.5 | 7.9 | 7.3 | 7.2 | 7.4 | 6.9 | 6.0 | 13.7 | 11.4 | 2.9 | 12.2 | 10.2 |
| MnO | 0.1 | 0.1 | 0.2 | 0.2 | 0.1 | 0.1 | 0.1 | 0.5 | 0.2 | 0.1 | 0.2 | 0.1 |
| MgO | 16.4 | 16.3 | 9.2 | 9.4 | 11.4 | 14.6 | 13.5 | 3.0 | 7.1 | 0.2 | 6.5 | 5.0 |
| CaO | 11.2 | 10.2 | 13.1 | 11.1 | 11.8 | 11.9 | 19.2 | 13.2 | 18.2 | 8.9 | 8.1 | 8.4 |
| $Na_2O$ | 0.9 | 0.9 | 3.1 | 2.9 | 2.2 | 1.6 | 0.5 | 3.2 | 2.4 | 5.5 | 4.5 | 4.6 |
| $K_2O$ | 5.8 | 6.7 | 4.7 | 5.6 | 5.6 | 5.1 | 5.7 | 3.3 | 1.5 | 4.0 | 2.5 | 1.1 |
| $P_2O_5$ | 1.2 | 2.5 | 1.2 | 1.0 | 1.4 | 1.6 | 3.4 | 0.6 | 2.8 | 0.1 | 0.7 | 0.3 |
| L.O.I | 3.4 | | 2.1 | | 1.4 | | | 0.2 | 1.0 | 4.2 | | |
| Total | 99.9 | 99.0 | 99.9 | 98.1 | 100.1 | 97.3 | 98.1 | 100.7 | 100.5 | 99.7 | 98.7 | 97.6 |
| Ni | 470 | 481 | 210 | 234 | 290 | 314 | 114 | <20 | 40 | <20 | 165 | 98 |
| Cr | 860 | 563 | 350 | 353 | 510 | | 21 | <20 | <20 | <20 | 213 | 166 |
| V | 177 | 181 | 158 | 183 | 162 | | 192 | 176 | 224 | 42 | 219 | 156 |
| Cs | 3.1 | 3.5 | 6.8 | 8.0 | 2.6 | | 1.4 | 1.3 | <0.5 | <0.5 | 0.8 | 0.5 |
| Rb | 199 | 220 | 145 | 188 | 167 | 184 | 82 | 58 | 13 | 66 | 47 | 27 |
| Ba | 3523 | 3547 | 2680 | 2847 | 3581 | | 2306 | 1271 | 1423 | 2457 | 513 | 297 |
| Sr | 3882 | 2958 | 4008 | 5785 | 3650 | 2959 | 5964 | 1990 | 3832 | 7449 | 1341 | 535 |
| Nb | 17 | 15 | 23 | 27 | 23 | 25 | 5 | 8 | 16 | 129 | 77 | 28 |
| Ta | 0.9 | 0.9 | 1.5 | 1.7 | 1.1 | | 0.4 | 1.5 | 0.6 | 4.7 | 4.8 | 5.6 |
| Zr | 361 | 224 | 367 | 379 | 482 | 551 | 112 | 343 | 245 | 649 | 218 | 174 |
| Y | 14 | 13 | 27 | 25 | 20 | | 16 | 21 | 38 | 26 | 22 | 18 |
| Hf | 7.8 | 7.0 | 7.3 | 10.0 | 9.7 | | 4.0 | 8.0 | 6.3 | 10.2 | 5.0 | 4.0 |
| Th | 13.3 | 8.0 | 28.9 | 26.0 | 27.1 | 10.2 | 5.0 | 32.0 | 19.5 | 156.0 | 6.0 | 2.0 |
| U | 2.6 | 2.6 | 11.3 | 13.5 | 6.6 | 12.0 | 1.1 | 7.9 | 3.5 | 73.6 | 1.0 | 1.0 |
| Pb | 26.0 | 30.0 | 123.0 | 151.0 | 74.0 | 37.8 | 28.0 | 34.0 | 15.0 | 85.0 | | 2.0 |
| La | 92.9 | 90.0 | 280.0 | 233.0 | 150.0 | 157.7 | 116.0 | 78.5 | 258.0 | 826.0 | 45.0 | 16.0 |
| Ce | 200.0 | 199.0 | 499.0 | 426.0 | 315.0 | 260.3 | 281.0 | 195.0 | 617.0 | 1380.0 | 87.0 | 37.0 |
| Pr | 23.8 | 24.0 | 51.5 | 45.0 | 36.1 | | 38.0 | 24.7 | 76.9 | 135.0 | 10.0 | 4.0 |
| Nd | 93.8 | 104.0 | 182.0 | 169.0 | 137.0 | | 180.0 | 101.0 | 312.0 | 425.0 | 41.0 | 20.0 |
| Sm | 13.9 | 17.0 | 23.4 | 23.0 | 18.9 | | 29.0 | 15.7 | 44.2 | 41.3 | 8.0 | 5.0 |
| Eu | 3.1 | 4.7 | 4.7 | 5.8 | 4.1 | | 7.0 | 3.0 | 8.8 | 6.8 | 2.4 | 1.8 |
| Gd | 8.1 | 14.3 | 13.4 | 23.0 | 10.4 | | 24.1 | 8.4 | 23.6 | 20.0 | 8.8 | 5.9 |
| Tb | 0.7 | 1.2 | 1.2 | 1.7 | 1.0 | | 1.8 | 0.9 | 2.2 | 1.3 | 1.0 | 0.8 |
| Yb | 0.9 | 0.8 | 1.6 | 1.8 | 1.3 | | 0.8 | 2.5 | 2.1 | 2.1 | 1.5 | 1.3 |
| Lu | 0.1 | 0.1 | 0.3 | 0.2 | 0.2 | | 0.1 | 0.6 | 0.3 | 0.4 | 0.2 | 0.2 |

[a] Average of previous studies (Sabzehei, 1984; Shishebore, 1993); major elements (27 samples); trace elements (10 samples); La and Ce (8 samples).

and colorless clinopyroxene phenocrysts in a groundmass of acicular clinopyroxenes, phlogopite, apatite and anorthoclase, with minor magnetite and dark glass, and a small volume of vesicles. Phlogopites in this sample are similar in composition to that in the extrusive tephrites (Table 4). Most of the phlogopites in this sample are poikilitic, containing small crystals of pyroxene and apatite, and many of the pyroxenes phenocrysts have sieve texture. Poikilitic phlogopite such as is observed in this samples is a characteristic of madupitic lamproites.

Three holocrystalline plutonic samples, none of which contain any phlogopite, include a pyroxenite granitoid (sample M8; Fig. 5B), with strongly pleochroic deep-green to brown aegirine–augite pyroxene, K-feldspar, Na-plagioclase, apatite, sphene, magnetite and zircon. Another (M9) contains pale-green clinopyroxene plus brown-green amphibole (Table 5), K-feldspar, Na-plagioclase, apatite and magnetite. A third holocrystalline sample is an anorthoclase pyroxentite (sample M11; Fig. 6A) which contains anorthoclase and sanidine (Table 3; and Fig. 7), less abundant dark-green aegirine–augite pyroxene (Table 2), and approximately 20 vol% modal calcite crystals similar in size to the anorthoclase and sanidine grains, along with minor REE-rich dark-brown allanite and britholite (Fig. 6B; and Table 6), magnetite, zircon and apatite. Calcite crystals contain small grains of clinopyroxene and apatite (Fig. 6A), indicating that the calcite co-precipitated with the other igneous minerals in this rock, and is not a secondary or replacement phase.

### 4.2. Whole rock chemistry

#### 4.2.1. Major elements

The major and trace element concentrations of the QHA extrusive rocks and associated plutonic xenoliths, and also the average composition of Neogene/Quaternary alkali olivine basalts erupted further north along the western margin of the Lut block, are listed in Table 7. All the QHA extrusive samples plot as basanaite tephrites in the alkalic field on a silica versus total alkali element content classification diagram (Fig. 8). The $K_2O$ versus $Na_2O$ (wt%) diagram shows that the alkali olivine basalts from the northern (NNF) and middle (MNF) parts of the Nayband fault belong to the Na-series, but the lavas from the QHA maars plot in the high K-series field (Fig. 9). The CaO contents of the QHA samples range from 10 to 13 wt%, while $SiO_2$ is <47 wt%. These values are typical of kamafugites, but not lamproites.

The extrusive samples exhibit negative correlations between MgO versus $SiO_2$, $Al_2O_3$, CaO and $Na_2O$, whereas $TiO_2$, FeO, $K_2O$ and $P_2O_5$ decrease with decreasing MgO (Fig. 10). The positive correlation between decreasing $TiO_2$ and $K_2O$ with decreasing MgO is interpreted as reflecting decreasing modal proportions of high

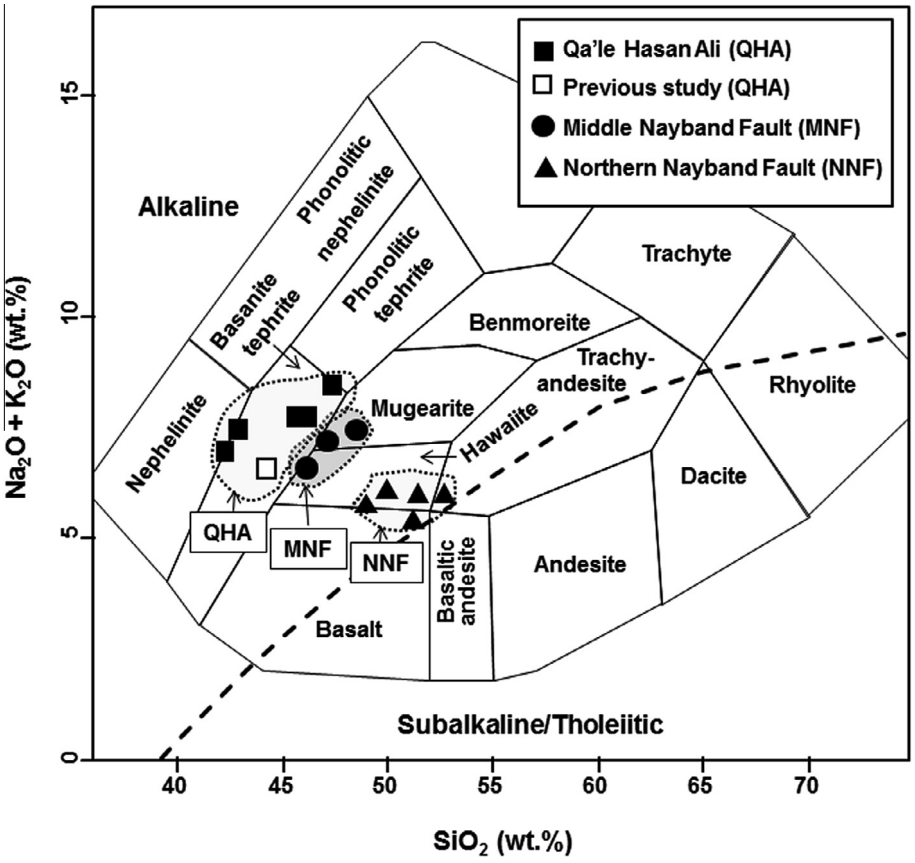


**Fig. 8.** $SiO_2$ versus total alkalies diagram (Cox et al., 1979) for samples from QHA (Table 7) compared to samples from Neogene/Quaternary alkali olivine basalts farther to the north along the Nayband fault (Fig. 1; Saadat et al., 2010). QHA samples plot in the field of basanite tephrites.

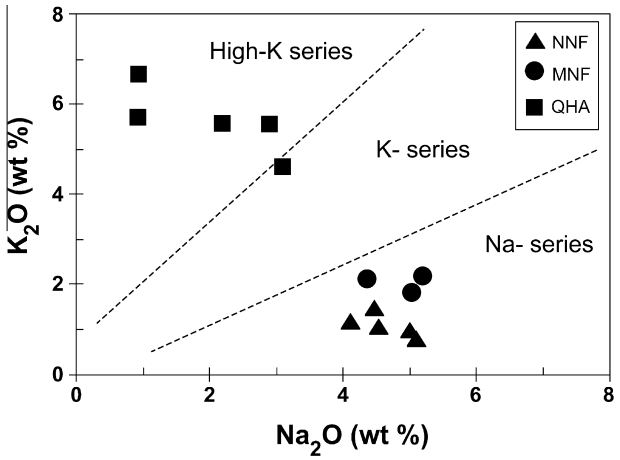


**Fig. 9.** $K_2O$ versus $Na_2O$ contents (Middlemost, 1975) of highly potassic QHA samples compared to those of Neogene/Quarternary Na-series alkali olivine basalts from farther north along the Nayband fault (MNF and NNF; Saadat et al., 2010).

Ti-phlogopite. The nearly holocrystalline samples (M1, M3 and M15; Table 7), which have higher modal proportions of phlogopite, are those with the higher $TiO_2$, MgO, $K_2O$ and lower $Na_2O$.

The plutonic rocks have variable major element compositions that reflect their different modal mineralogies. Those with a higher proportion of mafic minerals, such as M5 and M9, have lower $SiO_2$ and $Al_2O_3$ and higher CaO and MgO (Table 7). Samples M5 and M9 also have high concentrations of apatite and high $P_2O_5$. Sample M11, with a high modal proportion of calcite, has the highest LOI content, and high CaO relative to its low FeO and MgO contents, reflecting the calcite in the sample.

*4.2.2. Trace elements*

QHA extrusive samples have high Ni (210–470 ppm) and Cr (350–860 ppm) abundances typical of highly potassic MgO-rich volcanic rocks such as basanite tephrites, kamafugites and/or lamproites, and greater than the average concentrations of Ni and Cr in both Neogene/Quaternary alkali olivine basalts samples from farther north along the Nayband fault (Table 7), and ultrapotassic leucite basanites from the 11 Ma Saray volcano farther northwest along the northwest-southeast fault system on which the QHA maars occur (<60 and <220 ppm; Pang et al., 2013). The holocrystalline samples (M1, M3 and M15; Table 7), with higher MgO, also have higher Ni and Cr than the more glassy porphyritic samples.

The concentrations of large-ion-lithophile (LIL), some high-field-strength (HFS) and light rare-earth (LRE) element in the extrusive rocks are also high. Ba ranges from 2840 to 3580 ppm, Sr from 2950 to 5880 ppm, and Rb from 145 to 220 ppm, while Zr ranges from 220 to 480 ppm, and La from 90 to 280 ppm (Table 7). These concentrations are significantly higher than those of the Neogene/Quaternary intra-plate OIB-like alkali olivine basalts erupted farther north along the Nayband fault (Fig. 11), and they are consistent with geochemical criteria for the recognition of highly potassic tephrites, lamproites and kamafugites presented by Mitchell and Bergman (1991).

In contrast Nb, Ta, Y, Hf, U and heavy rare-earth (Yb) element contents are low, and similar to or lower than the Neogene/Quaternary alkali olivine basalts from farther north along the Nayband fault (Fig. 11; and Table 7). The highly potassic QHA extrusives have high La/Yb $\geqslant$ 100. Their low Nb and Ta contents relative to large-ion-lithophile elements (Ba, Rb, Sr, K and La) is distinct from OIB or intra-plate alkali olivine basalts in general, and more similar

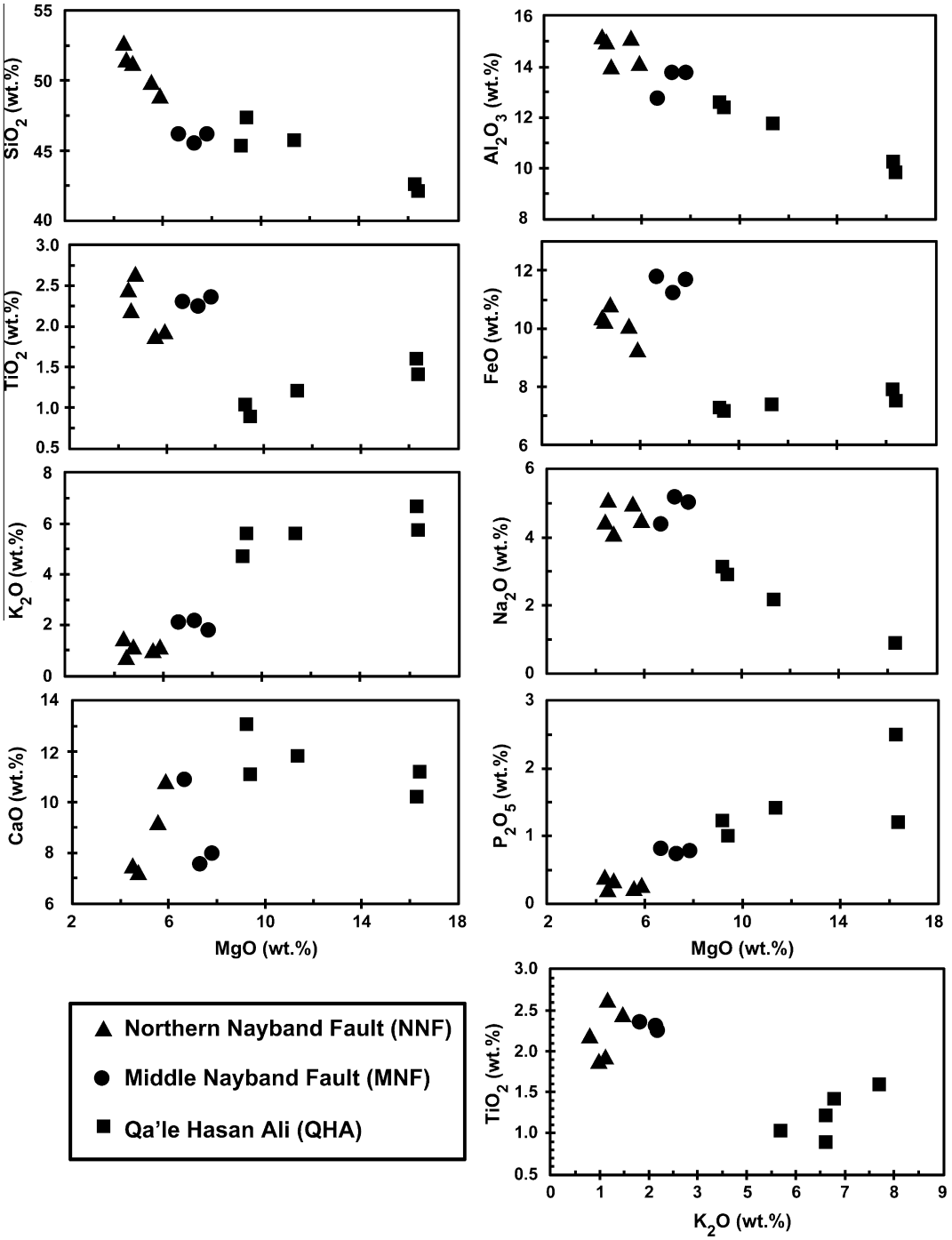


**Fig. 10.** Harker diagrams illustrating variations of major elements relative to MgO, and $TiO_2$ realtive to $K_2O$, for QHA tephrites and alkali olivine basalts from farther north along the Nayband fault (Saadat et al., 2010). Positive correlations among MgO, $TiO_2$ and $K_2O$ are interpreted to result from variations in the modal proportion of Ti-phlogopite in the different tephrite samples.

to convergent plate boundary volcanic arc magmas such as those erupted in the Makran arc to the southeast of QHA (Saadat and Stern, 2011). In this respect they are similar (Fig. 11) to phlogopite lamproites from Leucite Hills, WY (Mirnejad and Bell, 2006) and leucite basanites from the Saray volcano in northwest Iran (Pang et al., 2013), both of which formed in a post-collisional continental area which had previously experienced subduction-related arc volcanism, and also to leucite basanites from the Roman co-magmatic province (Rogers et al., 1985; Conticelli et al., 2009; Boari et al., 2009), which are related to subduction processes.

The concentrations of Ni, Cr, Cs, Rb and Ba are lower in the plutonic xenoliths than the extrusive rocks. Sample M11, which contains up to >20% modal calcite, has very high Sr, Nb, Ta, Zr, Th, U, and REE compared to both the extrusive rocks and other plutonic samples (Table 7), the high REE content reflecting the presences of ~3 modal percent REE-rich allanite and britholite (Fig. 6B; and Table 6) in the rock.

*4.2.3. Sr, Nd and Pb isotopic ratios*

The Sr and Pb isotopic composition of one extrusive (M15) and one plutonic sample (M11) are similar (Table 8; and Figs. 12 and 13), but the $\epsilon_{Nd}$ of the extrusive sample is somewhat lower than that of the plutonic rock. Both samples have Sr and Nd isotopic ratios that differ from most other Neogene/Quaternary igneous

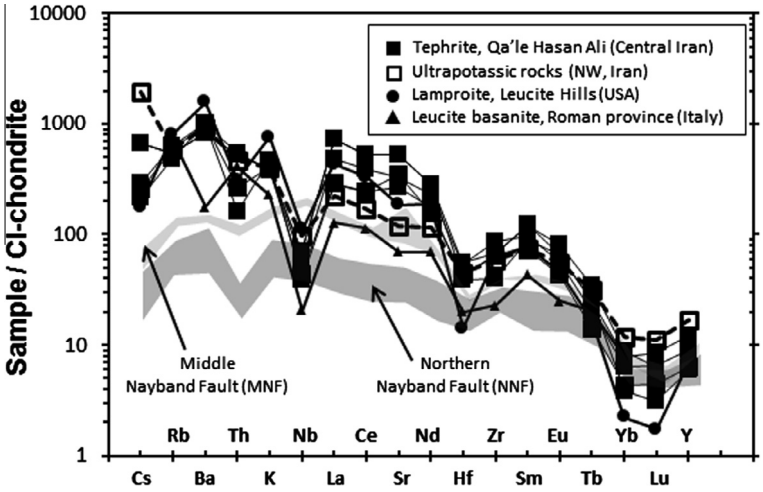


**Fig. 11.** Spider diagrams of trace-element concentrations, normalized to chondritic meteorites (from Gerlach et al., 1988), for QHA tephrites, phlogopite lamproites from Leucite Hills, Wyoming (Mirnejad and Bell, 2006), leucite basanites from the Roman volcanic province, Italy (Rogers et al., 1985; Conticelli et al., 2009; Boari et al., 2009) and the 11 Ma Saray volcano in northwestern Iran (Pang et al., 2013), and alkali olivine basalts from farther north along the Nayband fault (Saadat et al., 2010). Unlike the alkali olivine basalts, which have OIB-like intraplate chemical characteristics, the QHA tephrite and other ultra-potassic rocks plotted, which all formed in active subduction or post-collisional tectonic environments, have negative Nb and Ta anomalies compared to LIL and LREE. This suggests they formed from mantle metasomatized by aqueous fluids or magmas derived from subducted oceanic crust and sediments.

**Table 8**
Sr, Nd, and Pb isotopic compositions of Qa'le Hasan Ali samples and Neogene and Quaternary alkali basalts from farther north along the Nayband fault.

| Location | Sample no. | $^{87}Sr/^{86}Sr$ | $^{143}Nd/^{144}Nd$ | $\epsilon_{Nd}$ | $^{208}Pb/^{204}Pb$ | $^{207}Pb/^{204}Pb$ | $^{206}Pb/^{204}Pb$ |
|---|---|---|---|---|---|---|---|
| QHA | M-15 whole-rock | 0.705930 | 0.512464 | −3.4 | 38.498 | 15.582 | 18.458 |
| | M-11 whole-rock | 0.705836 | 0.512573 | −1.3 | 38.511 | 15.585 | 18.466 |
| | M-11 calcite | 0.705906 | | | | | |
| | M-11 leachate | 0.705907 | | | | | |
| | M11 anorthoclase | 0.705943 | | | | | |
| MNF[a] | Gg-1 | 0.704505 | 0.512730 | 1.8 | 38.972 | 15.596 | 18.975 |
| | GM-1 | 0.704590 | 0.512709 | 1.4 | 38.753 | 15.583 | 18.755 |
| NNF[a] | S2-3 | 0.705555 | 0.512728 | 1.8 | 38.409 | 15.556 | 18.470 |
| | S3-1 | 0.705312 | 0.512686 | 0.9 | 38.589 | 15.581 | 18.564 |

[a] Data from Saadat et al. (2010). MNF = Middle Nayband fault, NNF = Northern Nayband fault.

rocks in Iran, but although they have higher $^{87}Sr/^{86}Sr$ and lower $\epsilon_{Nd}$ than most other Iran volcanic rocks, these ratios are not as high or low, respectively, as those for the Miocene ultra-potassic 11 Ma Saray volcano in northwestern Iran (Pang et al., 2013) or the late Quaternary Khanneshin Carbonatite Complex in western Afganistan (Fig. 12; Tucker et al., 2012). However, the Pb isotopic ratios of the highly potassic QHA rocks and Khanneshin carbonatites are similar (Fig. 13).

For the plutonic sample M11, which contains 20 modal percent calcite, Sr isotopic ratios were determined for both the whole-rock as well as calcite and anorthoclase feldspar. These phases were both sampled by micro-drilling. All three samples, and also the leachate from the whole-rock leached in HCl, which is essentially calcite, have the same Sr isotopic composition (Table 8), consistent with the petrologic data that indicates that calcite is a magmatic phase in these rocks, co-crystallized with the other igneous minerals in the rock, and not a secondary or replacement phase.

## 5. Discussion and conclusions

### 5.1. Classification

Milton (1976–77) referred to the QHA extrusive rocks as highly potassic tephrites. With regard to silica and total alkali content they fall in the field of basanite tephrite (Fig. 8). Their high $K_2O$ relative to $Na_2O$ and the presence of Ti-phlogopite and Mg-rich olivine phenocrysts suggests affinities with the lamproite clan of rocks (Shishebore, 1993). However, these rocks lack leucite and contain minor accessory sodic phases such as both hauyne and analcime, which Mitchell and Bergman (1991) consider as not occurring in rocks of the lamproite clan as they define it. Also their $Al_2O_3$ (>10 wt%) and CaO (>10 wt%) contents are higher than most lamproites. Their high CaO and low $SiO_2$ are consistent with many of the features of kamafugites (Sabzehei, 1984), but they lack kalsilite and even leucite. Their relatively high $Al_2O_3$ and CaO is also similar to highly potassic Roman province leucite basanites. Essentially the QHA samples have compositions that bridge the range between chemical Group II (kamafugites) and Group III (Roman province) highly potassic rocks as defined by Foley et al. (1987).

With respect to trace elements the QHA samples have very high large-ion-lithophile (LIL) element enrichments, typical of most highly potassic magmas, but depletion in Nb and Ta relative to LIL elements and LREE (Fig. 11). Group III (Roman province) highly potassic magmas also have depletion in Nb and Ta relative to LIL and LREE, as do Miocene leucite basanites from the Saray volcano in northwest Iran and Quaternary phlogopite lamproites from Leucite Hills, WY (Fig. 11).

In summary the QHA samples are chemically and mineralogically distinct from lamproites (Group I of Foley et al., 1987) and kamafugites (Group II of Foley et al., 1987). They do not occur in a rift tectonic environment as do kamafugites. They may possibly be related to the Makran arc and processes associated to active subduction (see discussion below) as are Roman province highly

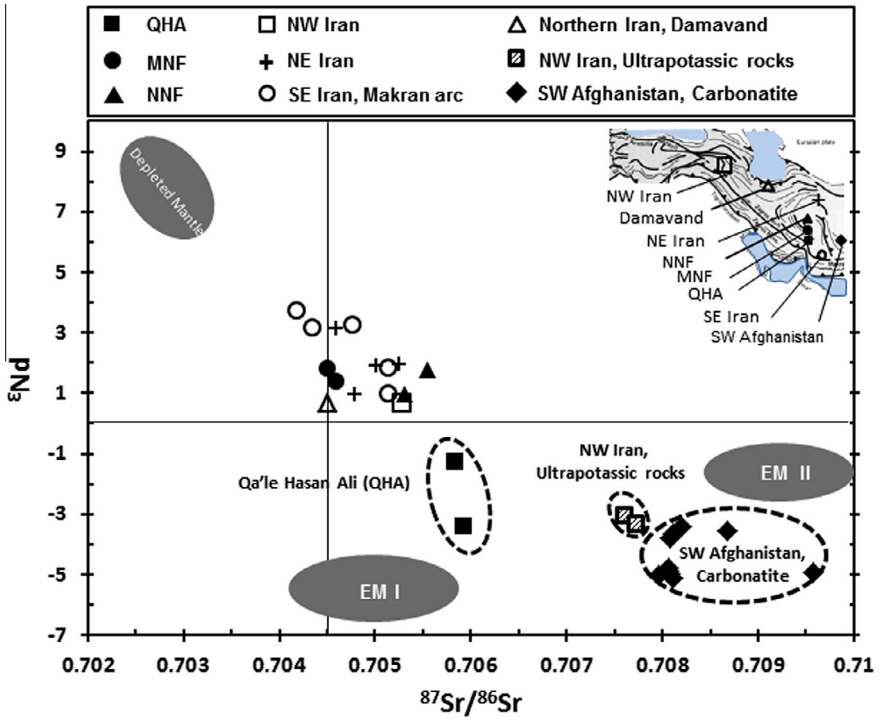


**Fig. 12.** $^{87}Sr/^{86}Sr$ versus $\epsilon_{Nd}$ for samples from QHA maars, compared to highly potassic rocks from Leucite Hills, Wyoming (Mirnejad and Bell, 2006) and Saray volcano in northwest Iran (Pang et al., 2013), the Khannishin Carbonatite in Afganistan (Tucker et al., 2012), and alkali olivine basalts from farther north along the Nayband fault (Saadat et al., 2010) and elsewhere in Iran (Alicic et al., 2002; Liotard et al., 2008; Saadat and Stern, 2011, 2012). Mantle fields from Hofmann (1997).

potassic rocks (Group III of Foley et al., 1987), and they certainly do occur in an area that was affected by subduction related magmatism in the geologically recent (Tertiary) past, as are many different types of post-collisional highly potassic rocks formed elsewhere along the Alpine–Himalayan collision zone. We believe that the best classification is the most general one proposed by Milton (1976–77), as highly potassic tephrites, or as basanite tephrites as indicated by their total alkali element versus silica content (Fig. 8).

### 5.2. Plutonic xenoliths

Some of the tephrite coated plutonic xenoliths found within the tuff rims of the maars are interpreted as cogenetic with the tephrites because of their similar mineralogy and isotopic compositions. Among these, the anorthoclase–pyroxenite sample M11 with ~20 modal percent calcite and ~3 modal percent REE-rich allanite and britholite is of particular significance. The calcite in this sample is considered to be magmatic calcite because of (1) its grain size, which is similar to both feldspars and aegirine–augite pyroxenes in these rocks (Fig. 6A), (2) the occurrence of fine-grained inclusions of pyroxene and apatite within calcite grains (Fig. 6A), and (3) the similarity of the isotopic composition of the calcite with the other minerals in this rock (Table 8). The fact that this magmatic calcite has remained intact and not volatilized during the transport of these xenoliths to the surface in the hot tephrite magma implies a short transit time, and suggests that they are samples of a shallow plutonic complex, as does the presence of anorthoclase in these plutonic xenoliths (Table 3; and Fig. 7). The high modal proportions of magmatic calcite in some samples suggests that this shallow plutonic complex has affinities with carbonatites. A number of other carbonatite complexes associated alkalic igneous rocks occur along the Alpine–Himalayan collision, including the Quaternary Khanneshin Carbonatite Complex in Afghanistan (Fig. 1; Mars and Rowan, 2011; Tucker et al., 2012) and the multiple mid-Tertiary carbonatite complexes in the Mainning-Dechang belt in China (Xu et al., 2003; Hou et al., 2009; Xie et al., 2009). Woolley and Kjarsgaard (2008) note that the occurrence of basanite tephrites with carbonatites is uncommon, but not unknown.

### 5.3. Petrogenesis

#### 5.3.1. Mantle source composition

The very high Ni and Cr abundances, high MgO content (Fig. 10), and the Mg-rich olivine in the QHA basanite tephrites implies a mantle origin for these rocks. Their relatively high CaO and $Al_2O_3$ contents compared to many highly potassic volcanic rocks such as lamproites suggests derivation from a fertile lherzolite peridotite rather than an infertile harzburgite. Their high LIL and LREE content and LREE/HREE ratio, and low HREE content, suggests that they formed by low degrees of partial melting of mantle in the garnet stability field, implying either the lower part of the continental lithosphere or underlying asthenosphere. Their high Sr, Nd and Pb contents imply that their isotopic compositions reflect that of their mantle source and not crustal contamination. As with highly potassic volcanic rocks occurring along the Alpine–Himalayan collision belt and elsewhere around the world, their isotopic compositions are unlike those of mid-ocean ridge or oceanic island basalts derived from convecting asthenospheric mantle (Figs. 12 and 13). Instead their isotopic compositions suggest either an ancient metasomatic enrichment of their mantle source by high Rb/Sr, Nd/Sm and U/Pb magmas or fluids, or a more recent metasomatic enrichment event by magmas or fluids derived from subducted pelagic, carbonate and/or terrigenous continental sediments. Their very high $K_2O$ and LIL element contents also imply metasomatic enrichment of their mantle source region. This metasomatized mantle source region is thus most likely to be the lower part of the non-convecting continental lithosphere, which either has accommodated the metasomatic components within vein networks, and/or has been transformed to phlogopite-bearing peridotite by the influx of K and LIL rich magmas or fluids.

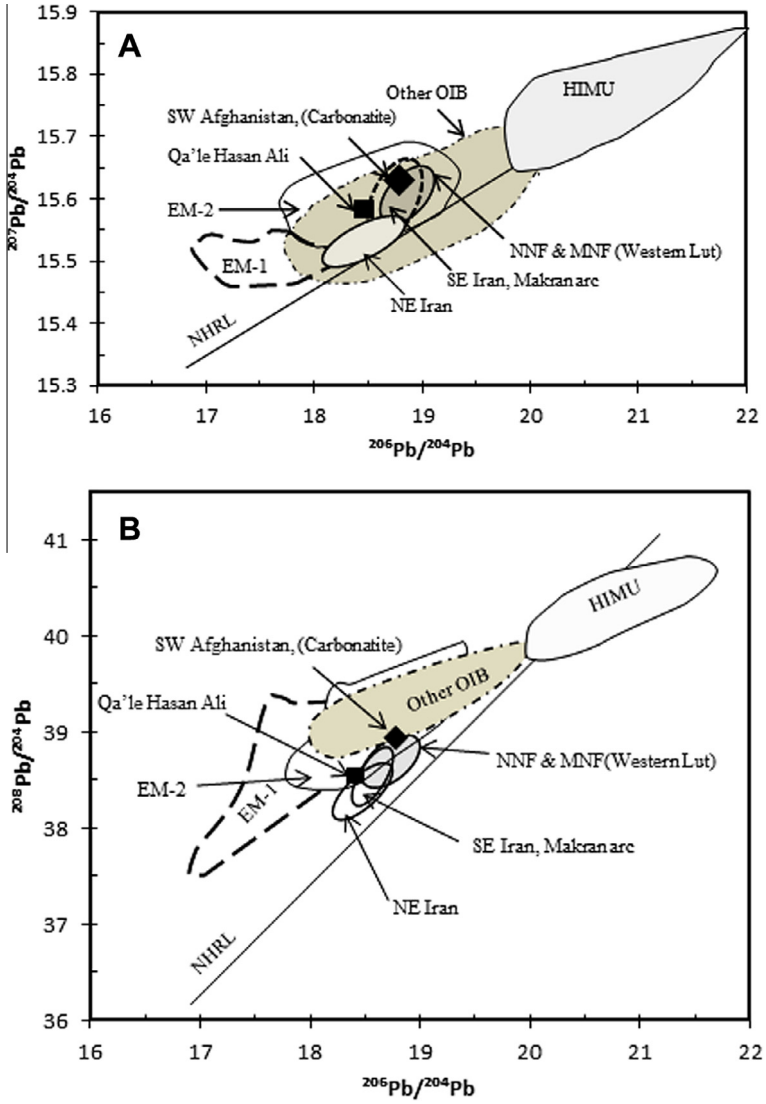


**Fig. 13.** Plot of $^{207}Pb/^{204}Pb$ and $^{208}Pb/^{204}Pb$ versus $^{206}Pb/^{204}Pb$. Sources from Saadat et al. (2010), Saadat and Stern (2011, 2012) and Tucker et al. (2012). Mantle fields from Hofmann (1997). NHRL = Northern Hemisphere Reference Line (Hart, 1984).

The QHA samples have very high large-ion-lithophile (LIL) element enrichments, typical of most highly potassic magmas, but depletion in Nb and Ta relative to LIL elements and light rare-earth-elements (LREE). Group III (Roman province) highly potassic magmas also have depletion in Nb and Ta relative to LIL and LREE (Fig. 11; Cox et al., 1976; Rogers et al., 1985; Peccerillo, 1985; Conticelli et al., 2009; Boari et al., 2009; Lustrino et al., 2011). This is interpreted to be due to their occurrence in an active subduction zone setting within which their enrichment in LIL is due to metasomatism of their mantle source, by hydrous fluids derived from subducted crust-derived sedimentary materials, with their relatively low concentrations of Nb and Ta being a result of the low solubility in aqueous fluids of these elements. Leucite basanites from the 11 Ma Saray volcano in northwestern Iran, and Quaternary phlogopite lamproites from Leucite Hills, WY, which both occur in an areas without active subduction, also have low Nb and Ta relative to LIL and LREE. In these cases, this is interpreted as due to low Nb and Ta relative to LIL and LREE in the subcontinental lithosphere inherited from mantle metasomatic processes which occurred when subduction was active below these areas in the late Cretaceous and Tertiary. The tectonic environments of both the Leucite Hills lamproites and Saray volcano leucite basanites are in this respect similar to that of the Quaternary post-collisional QHA maars, which occur in an area of extensive Eocene subduction related magmatism associated with the closure of the Neotethys ocean during the collision of the Arabian and Eurasion plates.

In summary, we consider the genesis of the highly potassic basanaite tephrites forming the QHA maars to be similar to that of other highly potassic post-collision volcanic rocks associated with the Alpine–Himalayan collision belt, such as those found at the 11 Ma Saray volcano and elsewhere in northwest Iran and Turkey (Ahmadzadeh et al., 2010; Pang et al.,; Allen et al., 2013), in many other areas of the western Mediteranean (Turner et al., 1999; Prelević et al., 2005, 2008, 2010, 2012; Conticelli et al., 2009; Lustrino et al., 2011; Tommasini et al., 2011), and in Tibet (Miller et al., 1999). This involved extensive metasomatic enrichment of the subcontinental lithospheric mantle by magmas and/or hydrous fluids derived from the subducted Neotethys oceanic plate, including crust-derived sediments.

The QHA basanite tephrites appear to be cogenetic with a shallow plutonic complex which has affinities with a carbonatite complex as evidences by high modal magmatic calcite in plutonic xenoliths entrained in the tephrites. Woolley and Kjarsgaard (2008) suggest that carbonatites associated with basanite tephrites are formed by processes of igneous differentiation from the highly potassic tephrite parental magma. The presence of a shallow

cogenetic plutonic complex with carbonatite affinities below the QHA maars indicates that the QHA tephrite magmas, and the fluids that metasomatized the lithospheric mantle source of these magmas, also contained $CO_2$, possibly derived from subducted carbonate sediments. High $CO_2$ contents have been shown to increase CaO in mantle melts (Edgar, 1987), which is a characteristic of the QHA tephrites compared to lamproites. Both $CO_2$ and CaO may have been added to the mantle source of these tephrites by subduction and devolitization of carbonate-rich sediments, as has been suggested for both Italian kamafugites (Avanzinelli et al., 2009; Boari et al., 2009; Conticelli et al., 2009), and other Alpine–Himalayan carbonatites (Xu et al., 2003).

*5.3.2. Causes of melting*

Recent mantle *Pn* tomographic velocity models for Iran indicate an area of relatively low *Pn* velocities, implying either high temperature or partial melting of the mantle below the area of the QHA maars (Al-Lazki et al., 2004; Lü et al., 2012). A number of different possible geodynamic causes of post-collisional mantle melting have been suggested for the generation of late Miocene to recent mafic magmas erupted in the general area of central and eastern Iran. These including (1) convective thinning and/or delamination of the thickened continental lithosphere below the collisional orogenic arc (Pearce et al., 1990; Shabanian et al., 2012; Pang et al., 2013); (2) slab roll-back and break-off and asthenospheric uprise through a slab window below the collisional arc (Shafiei et al., 2009; Ahmadzadeh et al., 2010; Agard et al., 2011; Shabanian et al., 2012; Pang et al., 2013); and/or (3) syn-collisional steepening of subduction angle, beginning as early as the Paleocene and/or Eocene (Saadat, 2010; Verdel et al., 2011; Agard et al., 2011), causing back-arc asthenospheric upwelling, extension, lithospheric thinning and magmatism over a broad zone northeast of the collisional arc.

The QHA maars intrude into calc-alkaline volcanic and plutonic rocks the Eocene Urumieh–Dokhtar magmatic belt, and therefore their generation by mechanisms that cause post-collisional asthenospheric uprise directly below this arc, such as delamination of the thickened lithosphere and/or post-collisional slab roll-back and break-off, are both reasonable possible causes for QHA magmatism. However, when considered in the larger regional picture of Lut block magmatism, which extended over a large distance northeast of the Urumieh–Dokhtar magmatic belt, and which diminished in volume and increased in alkalinity through time, specifically along the Nayband fault on the western margin of the Lut block (Saadat et al., 2010), a mechanism involving syn-collisional (Paleocene to late Eocene) steepening of the subduction angle of Neotethys oceanic lithosphere resulting in asthenospheric upwelling, lithospheric thinning and magmatism in the back arc can also explain the QHA maars as a very late expression of this larger long-lasting magmatic event.

An alternative possible explanation for the QHA maars is within the context of active subduction of Oman Sea lithosphere below southernmost Iran and the generation of the Makran arc (Fig. 1). Although the central part of the Makran arc consists of calc-alkaline stratovolcanoes (Saadat and Stern, 2011), these volcanoes become more alkaline to the east and the easternmost magmatic center along the trend of the arc is the Quaternary Khanneshin Carbonatite Complex in Afghanistan (Fig. 1; Mars and Rowan, 2011; Tucker et al., 2012), which contains leucite phonolites as well as REE-rich carbonatites. The QHA maars, in contrast, occur on the extreme western margin of the area of active subduction of Oman Sea lithosphere, at the intersections of the Oman line and Nayband fault zone. Although the western part of the Makran arc has little or no seismicity (Jackson et al., 1995), and the higher seismicity and large stratovolcanoes of the arc may result from the more rapid northwest convergence of the Omara microplate east of the Sonne fracture zone (Fig. 1), Oman Sea lithosphere is nevertheless being subducted below southern Iran as far west as the Oman line and Nayband fault. Therefore the QHA maars might represent the extreme western expression of this subduction process and Makran arc volcanism, just as the Khanneshin Carbonatite Complex in Afganistan may represent the extreme easternmost expression of this activity. The role of subduction in both these cases may be only to induce mantle convection and asthenospheric uprise above the slab, leading to thinning and melting of the subcontinental lithosphere already metasomatized during the closure of the Neotethys ocean.

*5.4. Summary conclusions*

The basanite tephrite of the Quaternary QHA marts in central Iran are part of an extensive belt of post-collisional highly potassic volcanic rocks associated with the Alpine–Himalayan belt stretching from Spain to Tibet. They may be underlain by a shallow plutonic complex with affinities with carbonatites and potentially economic REE mineralization, similar to other REE-rich carbonatite complexes associated with Alpine–Himalayan collision, including the Quaternary Khanneshin Carbonatite Complex in Afghanistan (Fig. 1; Mars and Rowan, 2011; Tucker et al., 2012) and the multiple mid-Tertiary carbonatite complexes in the Mainning-Dechang REE-belt in China (Xu et al., 2003; Hou et al., 2009; Xie et al., 2009). They formed by melting of a lower lithosphere mantle source metasomatized by fluids derived from subducted crustal sediments, including carbonate-rich sediments, during the closure of the Neotehtys ocean. They occur above an area of mantle with low *Pn*, consistent with mantle partial melting, and at the intersection of various large crustal structures which allowed the tephrite magmas to reach the surface from the mantle. A number of possible process may be responsible for this melting including post-collisional slab roll-back and break-off, delamination of the previously thickened continental lithosphere, continued but diminished asthenospheric uprise and lithospheric thinning in the back-arc region of the syn-collisional Eocene Urumieh–Dokhtar magmatic arc, and/or convective thinning of the lithosphere due to active subduction of Oman Sea lithosphere below the Makran arc area. We conclude, as Milton (1976–77) also concluded, that "this locality is worthy of further study for its significance in the Quaternary geologic development of Iran and for its petrologic peculiarities."

## Acknowledgements

We thank K. Mueller for help preparing the image in Fig. 1; J. Drexler and J. Allaz for assistance with the microprobe analysis, E. Verplank with help obtaining the isotopic analysis, E. Kamkar for assistance in the field, and the Geological Society of Iran, Kerman Branch, for access to internal reports. Comments by P. Verplank helped improve the final manuscript.

## References

Agard, P., Omrani, J., Jolivet, L., Whitechurch, H., Vrielynck, B., Spakman, W., Monié, P., Meyer, B., Wortel, R., 2011. Zagros orogeny: a subduction-dominated process. Geol. Mag. 148, 692–725.

Ahmadzadeh, Gh., Jahangiri, A., Lentz, D., Mojtahedi, M., 2010. Petrogenesis of Plio-Quaternary post-collisional ultrapotassic volcanism in NW of Marand, NW Iran. J. Asian Earth Sci. 39, 37–50.

Alicic, P., Temel, A., Gourgaud, A., 2002. Pb–Nd–Sr isotope and trace element geochemistry of Quaternary extension-related alkaline volcanism: a case study of Kula region (western Anatolia, Turkey). J. Volcanol. Geoth. Res. 115, 487–510.

Al-Lazki, A.I., Sandvol, E., Seber, D., Barazangi, M., Turkellii, N., Mohamad, R., 2004. Pn tomographic imaging of mantle lid velocity and anisotropy at the junction of the Arabian, Eurasian, and African plates. Geophys. J. Int. 158 (3), 1024–1040.

Allen, M.B., Kheirkhah, M., Neill, I., Emami, M.H., McLeod, C.L., 2013. Generation of arc and within-plate chemical signatures in collision zone magmatism: quaternary lavas from Kurdistan Province, Iran. J. Petrol. 54, 887–911.

Avanzinelli, R., Lustrino, M., Mattei, M., Melluso, L., Conticelli, S., 2009. Potassic and ultrapotassic magmatism in the circum-Tyrrhenian region: the role of carbonated pelitic vs. pelitic sediment recycling at destructive plate margin. Lithos 113 (1/2), 213–227.

Berberian, M., King, G.C.P., 1981. Towards a paleogeography and tectonic evolution of Iran. Can. J. Earth Sci. 18 (2), 210–265.

Boari, E., Tommasini, S., Laurenzi, M.A., Conticelli, S., 2009. Transition from ultrapotassic kamafugitic to sub-alkaline magmas: Sr, Nd, and Pb isotope, trace element and $^{40}Ar$–$^{39}Ar$ age data from the Middle Latin Valley volcanic field, Roman Magmatic Province. J. Petrol. 50 (7), 1327–1357.

Conticelli, S., Guarnieri, L., Farinelli, A., Mattei, M., Avanzinelli, R., Bianchini, G., Boari, E., Tommasini, S., Tiepolo, M., Prelević, D., Venturelli, G., 2009. Trace elements and Sr–Nd–Pb isotopes of K-rich, shoshonitic, and calc-alkaline magmatism of the Western Mediterranean Region: genesis of ultrapotassic to calc-alkaline magmatic associations in a post-collisional geodynamic setting. Lithos 107, 68–92.

Cox, K.G., Hawkesworth, C.J., O'Nions, R.K., Appleton, J.D., 1976. Isotopic evidence for the derivation of some Roman Region volcanics from anomalously enriched mantle. Contrib. Miner. Petrol. 56, 173–180.

Cox, K.G., Bell, J.D., Pankhurst, R.J., 1979. The Interpretation of Igneous Rocks. George Allen and Unwin, London, p. 450.

Edgar, A.D., 1987. Experimental petrology: inferences on the genesis of alkaline magmas with emphasis on their source regions. In: Fitton, G., Upton, B.G.J. (Eds.), The Alkaline Igneous Rocks. Geological Society, Special Paper 30, pp. 29–52.

Ercit, T.S., 2002. The mess that is "allanaite". Can. Mineral. 40, 1411–1419.

Esmaiely, D., Nédéléc, A., Valizadeh, M.V., Moore, F., Cotton, J., 2005. Petrology of the Jurrasic Shah-Kuh granite (eastern Iran), with reference to tin mineralization. J. Asian Earth Sci. 25, 961–980.

Farhoudi, G., Karig, D.E., 1977. Makran of Iran and Pakistan as an active arc system. Geology 5, 664–668.

Foley, S.F., Venturelli, G., Green, D.H., Toscani, L., 1987. The ultrapotassic rocks: characteristics, classification and constraints for petrogenetic models. Earth Sci. Rev. 24, 81–134.

Gerlach, D., Frey, F.A., Moreno-Roa, H., Lopez-Escobar, L., 1988. Recent volcanism in the Puheyue-Cordon Caulle region, southern Andes, Chile (40.5°S); Petrogensis of evolved lavas. J. Petrol. 29, 332–382.

Gojković, S.E., 1972. Qal'eh Hasan Ali impact craters area, south-central Iran. In: Geological Survey of Iran, Internal Report.

Golonka, J., 2004. Plate tectonic evolution of the southern margin of Eurasia in the Mesozoic and Cenozoic. Tectonophysics 381, 235–273.

Hart, S.R., 1984. A large-scale isotope anomaly in the Southern Hemisphere mantle. Nature 309, 753–757.

Hofmann, A.W., 1997. Mantle geochemistry: the message from oceanic magmatism. Nature 385, 219–229.

Hou, Z., Tian, S., Xie, Y., Yang, Z., Yuan, Z., Yin, S., Yi, L., Fei, H., Zou, T., Bai, G., Li, X., 2009. The Himalayan Mianning–Dechang REE belt associated with carbonatite–alkaline complexes, eastern Indo-Asian collision zone, SW China. Ore Geol. Rev. 36, 65–89.

Jackson, J., Haines, A.J., Holt, W.E., 1995. Accommodation of Arabia–Eurasia plate convergence in Iran. J. Geophys. Res. 100, 15205–15219.

Jung, D., Keller, J., Khorasani, R., Marcks, C., Baumann, A., Horn, P., 1984. Petrology of the Tertiary magmatic activity in the northern Lut area, east Iran. Neues Jahrbuch fur Geologie und Palaontologie Abhandlungen 160, 417–467.

Karimpour, M.H., Stern, C.R., Farmer, G.L., Saadat, S., Malekezadeh, A., 2011. Review of age, Rb–Sr geochemistry and petrogenesis of Jurassic to Quaternary igneous rocks in Lut Block, Eastern Iran. J. Geope 1, 19–36.

Liotard, J.M., Dautria, J.M., Bosch, D., Condomines, M., Mehdizadeh, H., Ritz, J.-F., 2008. Origin of the absarokite–banakite association of the Damavand volcano (Iran): trace elements and Sr, Nd, Pb isotope constraints. Int. J. Earth Sci. (Geol. Rundsch) 97, 89–102.

Lü, Y., Liu, B., Pei, Sh., Sun, Y., Toksöz, M.N., Zeng, X., 2012. Pn tomographic velocity and anisotropy beneath the Iran region. Bull. Seismol. Soc. Am. 102 (1), 426–435.

Lustrino, M., Duggen, S., Rosenberg, C.L., 2011. The Central-Western Mediterranean: Anomalous igneous activity in an anomalous collisional tectonic setting. Earth Sci. Rev. 104, 1–40.

Mars, J.C., Rowan, L.C., 2011. ASTER spectral analysis and lithologic mapping of the Khanneshin carbonatite volcano, Afganistan. Geosphere 7, 286–289.

McCall, G.J.H., 1997. The geotectonic history of the Makran and adjacent areas of southern Iran. J. Asian Earth Sci. 15 (6), 517–531.

McCall, G.J.H., 2002. A summary of the geology of the Iranian Makran. In: Clift, P.D., Kroon, D., Gaedicke, C., Craig, J. (Eds.), The Tectonic and Climatic Evolution of the Arabian Sea Region. Geological Society of London Special Publications 195, pp. 147–204.

Middlemost, E.A.K., 1975. The basalt clan. Earth-Sci. Rev. 11, 337–364.

Miller, C., Schuster, R., Klotzli, U., Frank, W., Purtscheller, F., 1999. Post-collisional potassic and ultrapotassic magmatism in SW Tibet: geochemical and Sr–Nd–Pb–O isotopic constrains for mantle source characteristics and petrogenesis. J. Petrol. 40, 1399–1424.

Milton, D.J., 1976. Qal'eh Hassan Ali Maars, Central Iran. Bull. Volcanol. 40 (3), 201–208.

Mirnejad, H., Bell, K., 2006. Origin and source evolution of the Leucite Hills Lamproites: evidence from Sr–Nd–Pb–O isotopic compositions. J. Petrol. 47, 2463–2489.

Mitchell, R.H., Bergman, S.C., 1991. Petrology of Lamproites. Plenum press, New York, p. 447.

Musson, R.M.W., 2009. Subduction in the Western Makran: the historian's contribution. J. Geol. Soc. Lond. 166, 387–391.

Pang, K.N., Sun-Lin Chung, S.L., Zarrinkoub, M.H., Khatib, M.M., Mohammadi, S.S., Chiu, H.Y., Chu, C.H., Lee, H.Y., Lo, C.H., 2012. Eocene–Oligocene post-collisional magmatism in the Lut-Sistan region, eastern Iran: Magma genesis and tectonic implications. Chem. Geol. 306–307, 40–53.

Pang, K.N., Chung, S.L., Zarrinkoub, M.H., Lin, Y.C., Lee, H.Y., Lo, C.H., Khatib, M.M., 2013. Iranian ultrapotassic volcanism at ~11 Ma signifies the initiation of post-collisional magmatism in the Arabia-Eurasia collision zone. Terra Nova 25, 405–413.

Pearce, J.A., Bender, J.F., De Long, S.E., Kidd, W.S.F., Low, P.J., Güner, Y., Saroglu, F., Yilmaz, Y., Moorbath, S., Mitchell, J.G., 1990. Genesis of collision volcanism in Eastern Anatolia, Turkey. J. Volcanol. Geoth. Res. 44, 189–229.

Peccerillo, A., 1985. Roman comagmatic province. Evidence for subduction-related magma genesis. Geology 13, 103–106.

Prelević, D., Foley, S.F., Cvetković, V., Romer, R.L., Downes, H., 2005. Tertiary ultrapotassic volcanism in Serbia: constraints on petrogenesis and mantle source characteristics. J. Petrol. 46, 1443–1487.

Prelević, D., Foley, S.F., Romer, R.L., Conticelli, S., 2008. Mediterranean tertiary lamproites: multicomponent melts in post-collisional geodynamics. Geochim. Cosmochim. Acta 72, 2125–2156.

Prelević, D., Akal, C., Romer, R., Foley, S.F., 2010. Lamproites as indicators of accretion and/or shallow subduction in the assembly of Southwestern Anatolia, Turkey. Terra Nova 22, 443–452.

Prelević, D., Akal, C., Foley, S.F., Romer, R.L., Stracke, A., van den Bogaard, P., 2012. Ultrapotassic mafic rocks as geochemical proxies for postcollisional mantle dynamics of lithosphere: the case of SW Anatolia-Turkey. J. Petrol. 53, 1019–1105.

Rogers, N.W., Hawkesworth, C.J., Parker, R.J., Marsh, J.S., 1985. The geochemistry of potassic lavas from Vulsini, central Italy and implication for mantle enrichment processes beneath the Roman region. Contrib. Miner. Petrol. 90, 244–257.

Saadat, S., 2010. Petrogenesis of Neogene basaltic volcanism associated with the Lut block, eastern Iran: implication for tectonic and metallogenic evolution. Ph.D. Thesis, University of Colorado, Boulder, USA, p. 226.

Saadat, S., Stern, C.R., 2011. Petrochemistry and genesis of olivine basalts from small monogenetic cones of Bazman stratovolcano, Makran arc, southeastern Iran. Lithos 125, 607–619.

Saadat, S., Stern, C.R., 2012. Petrochemistry of a xenolith-bearing Neogene alkali olivine basalt from northeastern Iran. J. Volcanol. Geoth. Res. 225–226, 13–29.

Saadat, S., Karimpour, M.H., Stern, C.R., 2010. Petrochemical characteristics of Neogene and quaternary alkali olivine basalts from the western margin of the Lut block, eastern Iran. Iran. J. Earth Sci. 2, 87–106.

Sabzehei, M., 1984. Petrogeneses and origin of late Quaternary alkaline–carbonatite magmatic activities in the Qa'le Hasan Ali Rayen area. In: Geological Survey of Iran, Internal Report, p. 143.

Shabanian, E., Acocella, V., Gioncada, A., Ghasemi, H., Bellier, O., 2012. Structural control on volcanism in intraplate post collisional settings: late Cenozoic to quaternary examples of Iran and Eastern Turkey. Tectonics 31 (T3013), 1–25.

Shafiei, B., Haschke, M., Shahabpour, J., 2009. Recycling of orogenic arc crust triggers porphyry Cu mineralization in Kerman Cenozoic arc rocks, southeastern Iran. Miner. Deposita 44, 265–283.

Shahabpour, J., 2005. Tectonic evolution of the orogenic belt in the region located between Kerman and Neyriz. J. Asian Earth Sci. 24, 405–417.

Shahabpour, J., 2007. Island-arc affinity of the Central Iranian Volcanic Belt. J. Asian Earth Sci. 30, 652–665.

Shishebore, F., 1993. Petrography, geochemistry and petrology investigation from Rayen Qa'le Hasan Ali lamproites rocks. M.Sc Thesis, Shahid Bahonar University of Kerman, Kerman, Iran, p. 128.

Tommasini, S., Avanzinelli, R., Conticelli, S., 2011. The Th/La and Sm/La conundrum of the Tethyan realm lamproites. Earth Planet. Sci. Lett. 301, 469–478.

Tucker, R.D., Belkin, H.E., Schulz, K.J., Peters, S.P., Horton, F., Buttleman, K., Scott, E.R., 2012. A light rare-earth element (LREE) resource in the Khanneshin carbonatite complex of southern Afghanistan. Econ. Geol. 107, 197–208.

Turner, S.P., Platt, J.P., George, R.M.M., Kelley, S.P., Pearson, D.G., Nowell, G.M., 1999. Magmatism associated with orogenic collapse of the Betic–Alboran domain, SE Spain. J. Petrol. 40 (6), 1011–1036.

Verdel, C., Wernicke, B.P., Hassanzadeh, J., Guest, B., 2011. A Paleogene extensional arc flare-up in Iran. Tectonics 30 (TC3008), 1–20.

Walker, R.T., Gans, P., Allen, M.B., Jackson, J., Khatib, M., Marsh, N., Zarrinkoub, M., 2009. Late Cenozoic volcanism and rates of active faulting in eastern Iran. Geophys. J. Int. 177, 783–805.

Woolley, A.R., Kjarsgaard, B.A., 2008. Paragenetic types of carbonatite as indicated by the diversity and relative abundances of associated silicate rocks: evidence from a global database. Can. Mineral. 46, 741–752.

Xie, Y.L., Hou, Z.Q., Yin, S.P., Simon, C.D., Xu, J.H., Tian, S.H., Xu, W.Y., 2009. Continuous carbonatitic melt-fluid evolution for a REE mineralization system: Evidence from inclusions in the Maoniuping REE deposit in the western Sichuan, China. Ore Geol. Rev. 36, 89–104.

Xu, C., Huang, Z.L., Liu, C.Q., Qi, L., Li, W.B., Guan, T., 2003. Geochemistry of carbonatites in Maoniuping REE deposit, Sichuan Province. Sci. China (Ser. D) 46, 246–256.